ELSEVIER

Coordination Chemistry Reviews
219–221 (2001) 1075–1112

COORDINATION CHEMISTRY REVIEWS

www.elsevier.com/locate/ccr

Excited electronic states of transition-metal dimers and the VBCI model: an overview

Felix Tuczek [a], Edward I. Solomon [b,*]

[a] *Christian-Albrechts Universität Kiel, D-24098 Kiel, Germany*
[b] *Department of Chemistry, Stanford University, Stanford, CA 94305, USA*

Received 29 January 2001; accepted 18 April 2001

Contents

Abstract 1075
1. Introduction 1076
2. 'Dimer bands' — SPEs or CT transitions? The case of $[Cu_2Cl_6]^{2-}$ [5] 1078
3. Exchange effects in LF states (A) — weak dimer coupling: Cu acetate [10] 1082
4. Shifts and splittings in CT states of bridged dimers: symmetrically peroxo and azido bridged copper systems, hemocyanin and the VBCI model [15,23,24] 1086
5. Excited-state ferromagnetic coupling: the case of ferromagnetically coupled Cu(II) azido dimers [33,30] 1096
6. Exchange effects in LF states (B) — strong coupling in spin-flip states: VBCI-evaluation of excited-state *J*s [9] 1098
7. Exchange effects in LF states (C) — interconfigurational transitions, strong coupling and mixed interactions: iron- and manganese-oxo dimers [7,12,16]. 1101
   7.1 Mn(III)–O–Mn(III) 1101
   7.2 Fe(III)–O–Fe(III) 1105
8. VBCI parameters of homovalent systems applied to the corresponding one-electron reduced binuclear complexes: relevance to electron transfer [16] 1108
9. Summary and conclusions 1110
Acknowledgements 1111
References 1111

Abstract

Applications of the Valence-Bond Configuration Interaction (VBCI) model to the electronic structure of transition-metal dimers are reviewed. This approach describes the shifts

* Corresponding author. Tel.: +1-415-723-9104; fax: +1-415-725-0259.
E-mail address: edward.solomon@stanford.edu (E.I. Solomon).

PII: S0010-8545(01)00382-4

and splittings of ground and excited electronic states within a configuration interaction scheme. In particular, it allows a correlation of the magnetic properties of the electronic ground state (ferro- or antiferromagnetic coupling) to shifts and splittings in excited (and ligand-field) charge-transfer states which can be probed by optical absorption spectroscopy and magnetic circular dichroism. The review correlates the VBCI description to earlier approaches to describe dimer interactions (coupled-chromophore model, Tanabe-model, transition-dipole vector coupling) and makes the connection to the treatment of mixed-valent systems.

Keywords: Excited electronic states; Transition-metal dimers; VBCI model

1. Introduction

Understanding the influence of intermolecular interactions on the magnetic and spectroscopic properties of multinuclear transition-metal centers has been of long-standing interest in inorganic chemistry. This goal has gained additional significance due to the presence of metal clusters in biological systems. Metalloproteins containing multinuclear active sites with, e.g. copper, iron or manganese exhibit unique ground-state properties and excited-state spectral features which are associated with interactions between the metal centers. The most simple example of this problem is provided by the coupling of two mononuclear coordination units ('monomers') to a binuclear complex ('dimer'). Mostly, research has focused on the evaluation and theoretical interpretation of the isotropic exchange splitting $-2J$ between the total spin sublevels of the ground-state manifold being described by the spin Hamiltonian

$$H = -2J\hat{S}_1 \cdot \hat{S}_2 \tag{1}$$

where $\hat{S}_1$ and $\hat{S}_2$ are local spin operators on metal centers 1 and 2 and J is the ground-state magnetic coupling constant [1].

The excited states of binuclear transition-metal systems have also been known to exhibit effects due to dimer interactions [2]. Thus, high-intensity low-energy 'dimer bands' which are absent in the respective monomer spectra have been found in the absorption spectra of binuclear copper [3–5] and iron-oxo complexes [6,7] and recognized to be due to dimer interactions. Several possible assignments for these bands have been considered, including $d \rightarrow d$ simultaneous pair excitations (SPEs) and low-energy charge-transfer (CT) transitions. With respect to d–d spectra, intensity enhancement of ligand-field (LF) transitions of Mn(II) [8], Cr(III) [9] and other dimer combinations has also been a well-known effect of binuclear interactions. Energy splittings in the spin-flip excited states of these systems have been analyzed in terms of a Heisenberg Hamiltonian (1) with the exchange constant J now relating an excited state on one half of the dimer interacting with the ground state on the other half. However, this formalism did not provide a description of exchange interactions in excited states of orbital configurations different from that

of the ground state which, e.g. applies to all LF excited states of Cu(II) dimers. It has been shown that in this case the dimer splitting of each excited state depends on additional interactions which probe individual superexchange pathways between different combinations of d-orbitals [10].

Likewise, dimer formation has been found to have profound effects on the CT spectra of transition-metal systems [11–13]. Interest in this topic has been stimulated by the fact that a number of biologically important ligands are able to coordinate to metal centers in a variety of binding modes including different bridging structures. Particular effort has been directed towards an analysis of the correlation between binding geometry and CT spectrum. An important aspect of these studies has been to understand how for a particular binding mode the monomer CT spectrum changes upon going to the bridged dimer. From group theory, each monomer transition splits into two transitions in the dimer. The first evidence for this type of dimer splitting was observed in a spectral comparison between an end-on terminally azido coordinated Cu(II) complex and the corresponding *cis* μ-1,3 azido bridged dimer [14]. In addition if the dimer contains metal centers with unpaired electrons, each CT excited state further exhibits a magnetic splitting due to coupling of a single electron in a ligand orbital with the paramagnetic metal center(s). For binuclear Cu(II) centers, for example, each excited monomer state splits into four excited states in the dimer, two singlets and two triplets. It has been found that the CT singlet states exhibit a large shift to lower energy which can be considered as a large antiferromagnetic (AF) interaction in the CT excited state. Based on a detailed study of $[Cu_2Cl_6]^{2-}$, the above-mentioned 'dimer bands' have, in fact, shown to be such singlet–singlet CT bands shifted to low energy by large excited-state antiferromagnetism [5]. A Valence Bond Configuration Interaction (VBCI) model has been developed which accounts for all of these effects in terms of a number of electron transfer integrals (i.e. covalent interactions) which within a minimum active space couple ground state (GS), CT and MMCT (metal–metal-CT) states [15]. Importantly, this model in addition to explaining the excited-state spectroscopic features of bridged dimers also allows evaluation of the CT excited-state contributions to the magnetic coupling constant of the electronic ground state and thus correlates excited-state effects with ground-state properties. This in particular allows us to directly experimentally probe the various superexchange pathways involved in the ground-state magnetic coupling.

Although developed for CT states of bridging ligands, the VBCI model also has been applied to evaluate and interpret the exchange interactions in LF excited states of dimers. This relates to a VBCI analysis of the exchange interactions in spin-flip states [9] as well as to the analysis of LF states in binuclear oxo-bridged Mn [16] and Fe systems [7]. Further, the evaluation of VBCI parameters in a homobinuclear dimer has been shown to be of direct relevance to the determination of the electronic coupling matrix element mediating electron transfer in the corresponding one-electron reduced species [16]. This can already be achieved based on a determination of the J value of the homodimer. In view of this broadened scope, it appeared timely to present a short overview of the VBCI model along with the traditional approaches to ground- and excited-state interactions in dimers. In this

overview, characteristic examples of the different aspects of binuclear interactions in excited states of dimers are presented along with their theoretical interpretation in a mostly qualitative way, highlighting the role of the VBCI model as a theoretical basis for understanding these excited-state effects and their relevance to physical and chemical properties of the electronic ground state.

2. 'Dimer bands' — SPEs or CT transitions? The case of $[Cu_2Cl_6]^{2-}$ [5]

In order to experimentally characterize the effects of binuclear interactions in the excited states of Cu(II) dimers, Desjardins et al. carried out a detailed spectroscopic investigation of a series of binuclear chlorocuprates with different symmetries around the Cu(II) centers (Scheme 1) [5]. Analysis of the spectral data on the LF transitions of the mono- and binuclear systems clearly indicated that the d–d transitions are not significantly perturbed by the binuclear electronic structure. The observed increase in the LF transition intensity was rather found to arise from the lower symmetry of the two Cu(II) ion sites in the binuclear structure. In contrast, new spectral features were observed at about 20 000 cm^{-1} in the binuclear systems which are absent in the monomer spectra (Fig. 1). From the temperature dependence of their intensity, these 'dimer bands' were identified as singlet → singlet transitions. For the square-pyramidal C_{2h} dimers $((CH_3)_2NH_2)CuCl_3$ and $LiCuCl_3{\cdot}2H_2O$, they were further shown to be cleanly X- (i.e. Cu–Cu–) polarized. The large difference in polarization between these dimer bands and that of $KCuCl_3$ (tetragonal Cu(II) center) indicated that their intensity could not be due to a vibronic mechanism but had to relate to an electric-dipole allowed transition in the appropriate effective dimer symmetry.

Two possible assignments for theses 'dimer bands' were considered: SPE corresponding to one-photon excitation of a LF transition on both Cu(II) centers which is made allowed by the exchange interaction, and a ligand → metal CT transition that is found at considerably lower energy in the dimer relative to the monomer. The lowest-energy SPE transition being compatible with the Cu–Cu (X) polarization in the square-pyramidal dimers involves the $z^2 \rightarrow xy$ transition on one Cu and the $x^2 - y^2 \rightarrow xy$ transition on the second Cu(II) (throughout this review, a $d_n = n$ notation will be used). The observed X, Y polarization of the identical pair transition in $KCuCl_3$ requires a lower effective dimer symmetry ($D_{2h} \rightarrow C_i$). Based

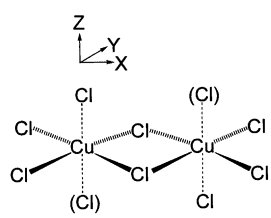

Scheme 1.

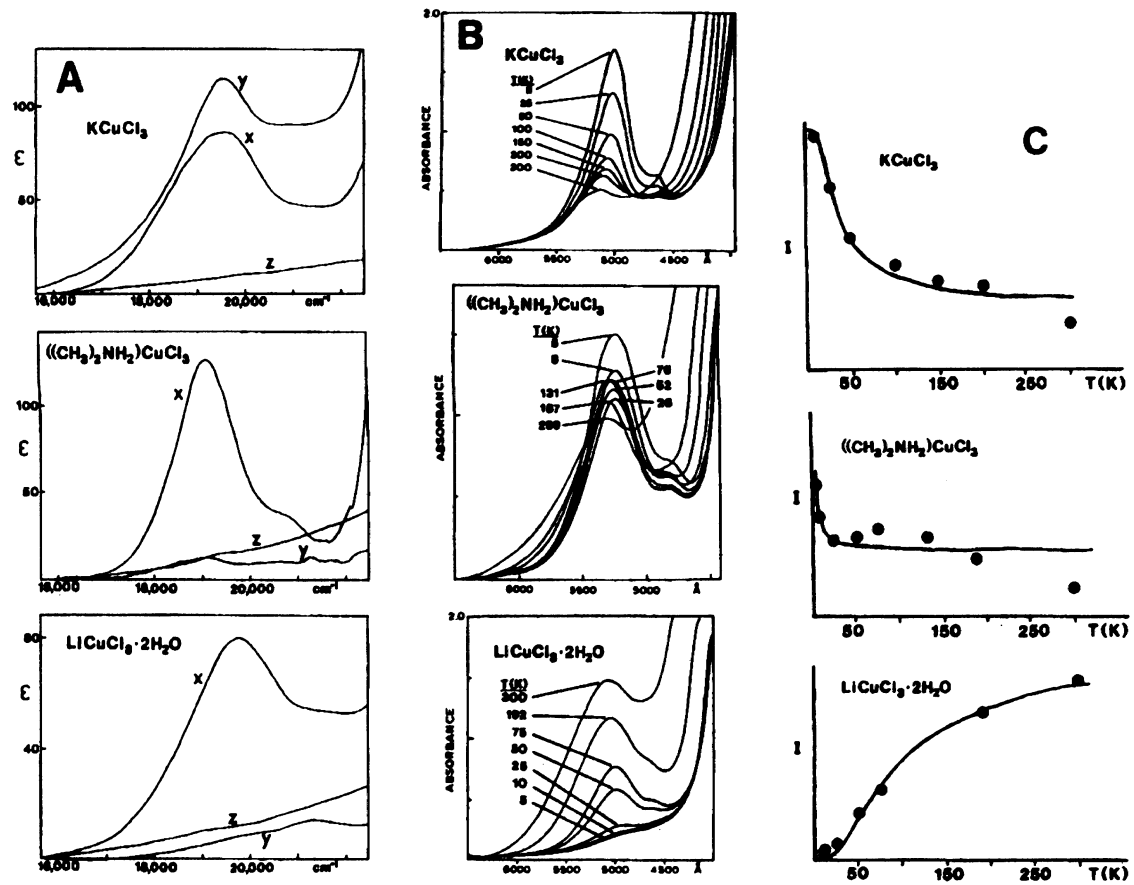

Fig. 1. Dimer bands in various Cu_2Cl_6 systems. (A) Molecular-polarized absorption spectra of the dimer bands: (upper) $KCuCl_3$ (210 K); middle $((CH_3)_2NH_2)CuCl_3$ (7 K); (lower) $LiCuCl_3{\cdot}2H_2O$ (192 K). (B) Temperature-dependent spectra for these systems. (C) Plots of the integrated intensity (I) of the dimer bands vs. temperature. Solid line: theoretical fit. Taken from Ref. [5].

on the following three pieces of evidence, however, the assignment of the dimer bands in the chlorocuprate systems to SPEs could be eliminated:

1. From an earlier spectroscopic study of Yb_2O_3, the band shape of an SPE was shown to depend on the product of the squares of the vibrational overlap integrals of the two independent LF excitations and therefore on the sum of the corresponding Huang–Rhys parameters $S_{(d\rightarrow d)A}$ and $S_{(d\rightarrow d)B}$, provided that the vibrational frequencies are similar in the monomer and dimer [17]:

$$S_{SPE} = S_{(d\rightarrow d)A} + S_{(d\rightarrow d)B} \quad (2)$$

   Experimentally it was found that the Huang–Rhys parameter of the $KCuCl_3$ dimer band (4.3) is of magnitude similar to those of the single-ion LF transitions (ca. 4) and about half of the expected sum (ca. 8); i.e. the dimer transition in $KCuCl_3$ is too sharp relative to that predicted for a SPE strongly arguing against this assignment.
2. Based on the single-ion transition energies, the dimer band in $KCuCl_3$ is 2600 cm^{-1} lower in energy than predicted for the SPE assignment ($E_{SPE} = E_{z^2\rightarrow xy} + E_{x^2-y^2\rightarrow xy} = 22\,500\ cm^{-1}$ vs. $E_{dimer} = 19\,950\ cm^{-1}$). This large energy deviation is unreasonable for a SPE transition.
3. The experimental results mentioned above indicate that the dimer bands are parity-allowed singlet → singlet transitions. Importantly, no indications of corresponding triplet → triplet dimer bands could be found although in principle such transitions should be observable from the small splitting of the ground state. This is dramatically illustrated in Fig. 1 where $KCuCl_3$ (top) has an antiferromagnetic and $LiCuCl_3{\cdot}2H_2O$ (bottom) a ferromagnetic ground state. In the former case, the dimer band appears at low temperature whereas in the latter case it disappears. The magnetic behaviour of $((CH_3)_2NH_2)CuCl_3$ (middle of Fig. 1) is complex and shows contributions from both intra- and interdimer effects. In all cases, the intensity of the dimer band could be correlated with population of the singlet ground-state component (Fig. 1, right). Therefore, in terms of the SPE assignment, the corresponding parity-allowed triplet pair transitions would either have to be significantly higher in energy ($> 3000\ cm^{-1}$) and obscured by the more intense CT transitions, or would have to lack an intensity mechanism available to the singlet transitions. The former possibility would correspond to an AF interaction in the SPE state which is not reasonable as it would require coupling a hole in the z^2-orbital on one Cu(II) to a hole in the x^2-y^2 orbital on the other Cu(II) center which would give rise to a ferromagnetic (orthogonal) exchange situation. The second possibility can also be excluded. A singlet only intensity mechanism could indeed be provided by configuration mixing of the SPE with the lowest-energy Cu(II)-to-Cu(II) (MMCT-) state which is necessarily a singlet. However, this gives rise to only an X-polarized transition and cannot account for the somewhat larger Y-(Cl–Cl–) polarization intensity observed in the singlet dimer transition of $KCuCl_3$ without an unreasonably large C_i site distortion of the Cu(II)s in the Y direction. Further, this Cu(II) → Cu(II) MMCT intensity mechanism would predict that, for the C_{2h} dimers like $((CH_3)_2NH_2)CuCl_3$, the dimer band should gain some

Z-($\perp$Cu–$(Cl)_2$–Cu) polarized singlet intensity from CI mixing, and this is not observed.

In contrast, assignment of the dimer bands to the singlet–singlet CT transition of a bridging chlorine-type MO to Cu(II) on one half of the dimer was shown to be consistent with the experimental findings. As the corresponding spin- and parity-allowed, triplet $\rightarrow$ triplet transition should have an intensity comparable to the allowed singlet but is not observed in any of the dimers within 3000 cm^{-1} of the singlet–singlet transition, this triplet excited-state has to be at least 3000 cm^{-1} higher in energy than the corresponding singlet excited state in all dimer salts. This indicates that the singlet excited state is stabilized by more than 3000 cm^{-1} with respect to the corresponding triplet excited state which explains the appearance of the singlet $\rightarrow$ singlet transition in the UV–vis absorption spectrum of the dimer, in contrast to the monomer. This large singlet stabilization can be rationalized from the overlap of the nonorthogonal orbitals associated with each $CuCl_4^{2-}$ 'half' of the dimer in the nonbonding π CT excited state (Fig. 2): CT excitation at, e.g. Cu_B produces a hole in the a_{2g}-orbital extending over its four chloride ligands. The two bridging-chloride orbital components have good overlap with the xy-orbitals on Cu_A, and this overlap should strongly stabilize the singlet relative to the triplet excited state.

This way, the Cu_2Cl_6 system has provided the first example where an unambiguous assignment of dimer bands to singlet–singlet CT transitions of bridging ligands, as opposed to SPEs, was achieved, implying that the energy of singlet CT excited state is drastically lowered with respect to the corresponding triplet by direct overlap between a metal orbital containing an unpaired electron and the bridging ligand orbital being singly occupied in the CT excited state. In terms of the VBCI model, this AF interaction in the CT state is described by CI with the MMCT state (cf. Section 4) which also accounts for the polarization observed for this type of dimer band.

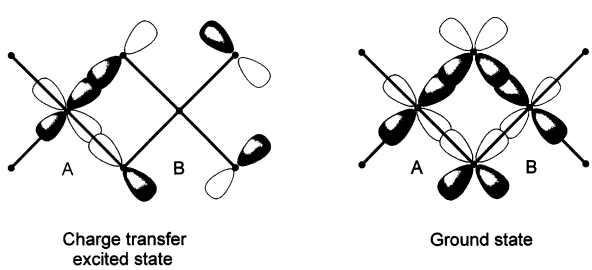

Fig. 2. Half-occupied orbitals on Cu_A and Cu_B associated with (left) the one-electron charge-transfer excited state originating from the a_{2_g} ligand-centered orbital on one 'half' ($Cu_BCl_4^{2-}$) of the $Cu_2Cl_6^{2-}$ dimer, and (right) the ground state of the $Cu_2Cl_6^{2-}$ dimer (adapted from Ref. [5]).

3. Exchange effects in LF states (A) — weak dimer coupling: Cu acetate [10]

Cu acetate (Scheme 2) played a historical role in inorganic chemistry as it was the first transition-metal dimer whose ground-state magnetic properties were evaluated in terms of an AF coupling between the two $S = 1/2$ metal centers giving rise to an $S = 0$ ground and $S = 1$ excited term being split by $-2J$ [18]. Likewise, the detailed interpretation of the LF spectra of the copper acetate system has been a classical problem of inorganic spectroscopy. There are three $d \rightarrow d$ transitions involving excitation from filled d-orbitals (z^2, xy, xz/yz) into the half-filled $x^2 - y^2$ orbital. As singly excited states can be equally reached on the left or on the right-hand side of the dimer, they are all doubly degenerate and in the presence of intradimer interactions split into symmetric/antisymmetric components ('sym/antisym' or 'g/u' splitting). Using a combination of linearly polarized absorption, variable-temperature MCD, and Zeeman spectroscopies, Ross et al. were able to assign ten LF excited states and directly evaluate the energy splittings between the dimer components of each LF transition [10]. They adopted the coupled-chromophore approach of Ballhausen and Hansen which treats the dimer as being composed of two independent units (in zeroth order) that each have a number of excited states and corresponding electronic transitions [19].

Fig. 3 shows the low-temperature optical absorption spectrum of Cu acetate including LF bands A–I and the dimer band at 26 000 cm^{-1}. In agreement with the results obtained on $[Cu_2Cl_6]^{2-}$, the dimer band has been assigned as a singlet → singlet LMCT band (cf. Section 2). The LF spectrum has been analyzed based on the energy diagram given in Fig. 4. For the d^9 configuration of each Cu(II) center a (one-) hole description can be applied that inverts the usual d-orbital energy level scheme. Therefore the b_1 ($x^2 - y^2$) level, corresponding to the hole in the highest singly occupied atomic orbital $x^2 - y^2$, lies at lowest energy and d-electron excitations from the lower lying, doubly occupied orbitals d_n (i.e. z^2, xy, and xz/yz) into $x^2 - y^2$ transfer the hole into d_n generating excited hole states at the corresponding d–d transition energies (Fig. 4, left). Upon going from the monomer to the dimer, each LF excited state d_n splits into a symmetric (g) and antisymmetric (u) combination as described above; moreover, the single hole in the d_n excited state couples magnetically with the hole in the $x^2 - y^2$ ground state at the other half of

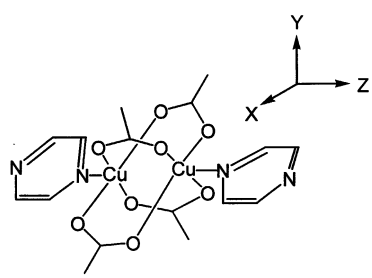

Scheme 2.

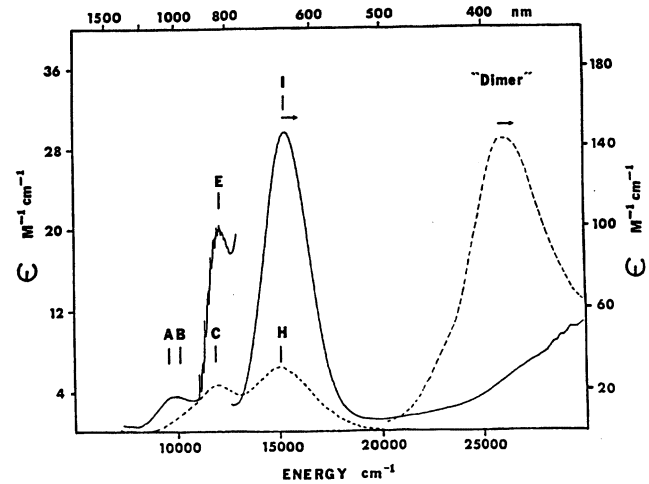

Fig. 3. Low-temperature (5 K) absorption spectra of Cu acetate pyrazine polarized along the molecular x, y (—) and z (- - -) directions. The letters indicate the positions of assigned ligand-field transitions. Band I and dimer intensities are defined by the right-hand scale (taken from Ref. [10]).

the dimer generating an excited singlet and an excited triplet state both of which then split into g/u combinations (Fig. 4, right). Taken together, each excited single-site LF state thus splits into four states in the dimer.

By evaluation of the eigenvalues of the Hamiltonian

$$H = h(1) + h(2) + e^2/r_{12} \tag{3}$$

using symmetry-adapted (two-hole) dimer wavefunctions, it follows that the splitting of each LF excited level into dimer states can be described by four parameters: K, J, L and I (Fig. 5). The Coulomb interaction K represents the average energy shift of the excited state from the monomer to the dimer, the exchange interaction J splits the excited state into singlet and triplet states, and the excitation transfer interactions I and L split the singlets and triplets into g/u components. With respect to a physical understanding of the meaning of these parameters (cf. Fig. 6):

1. The Coulomb matrix element K has contributions from both one-electron operators $h(i)$ and the two-electron operator e^2/r_{12} and adds equally to all four states. This produces a general offset of the dimer with respect to the monomer LF excited state. This is on the order of the two-electron (Coulomb) matrix element since evaluation of the one-electron matrix elements of H in the singly excited state d_n of the dimer just reproduces the energy of the corresponding excited state of the single-ion site. Note for the calculation of d–d transition energies that the ground state of the dimer is subject to a K interaction as well.
2. In the limit of non-overlapping (or orthogonal) single-site orbitals, J is a purely electrostatic exchange integral (operator e^2/r_{12}) and thus intrinsically positive ($J > 0$). Nevertheless, the coupled-chromophore analysis of Cu acetate shows that the J_{n,x^2-y^2} integrals vary from strongly antiferro- ($-2J_{x^2-y^2,x^2-y^2} = 325$)

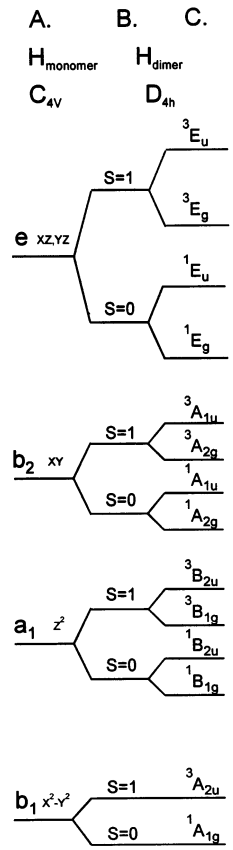

Fig. 4. Energy level diagram for copper acetate. Column A: splitting of copper d-orbitals in the effective C_{4v} symmetry of the monomer. Column B: singlet triplet splitting in the dimer; Column C: g/u splitting in the dimer (adapted from Ref. [10]).

over weakly antiferro- ($-2J_{xy,x^2-y^2}=50$) to moderately ferro- ($2J_{xz/yz,x^2-y^2}=125$) and strongly ferromagnetic ($2J_{z^2,x^2-y^2}=250$), respectively (all values in cm^{-1}). The fact that the 'symmetric' ground-state coupling constant $J_{x^2-y^2,x^2-y^2}$ is found to be negative clearly results from orbital overlap between the two subunits A and B that give rise to AF contributions to the ground-state $-2J$ value. This can be taken into account by, e.g. choosing nonorthogonal single-site orbitals that contain contributions from the bridging ligands [20]. This argument, on the other hand, cannot explain the negative sign of the 'asymmetric' or 'mixed' excited-state coupling constant J_{xy,x^2-y^2}. However, inclusion of spin-orbit coupling will allow the ground state to mix with the xy and xz/yz excited states, respectively, producing a non-zero AF contribution to J_{n,x^2-y^2}. The experimentally determined excited-state J values then reflect the competition between this AF and the ferromagnetic contribution from the e^2/r_{12} term. Likewise the experimentally determined J_{xy,x^2-y^2} and $J_{xz/yz,x^2-y^2}$ constants

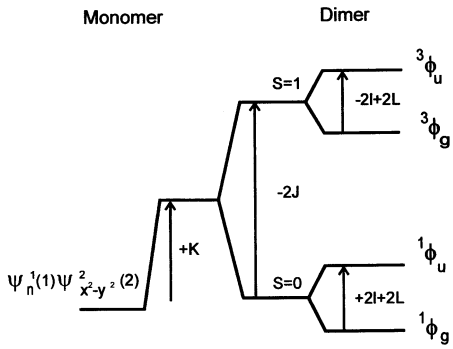

Fig. 5. Monomer to dimer excited-state splitting diagram. The Coulomb interaction (K) represents an average energy shift from the monomer to the dimer. The exchange interaction (J) splits the excited state into singlet and triplet states. The excitation transfer interactions (I and L) split the singlets and triplets into g–u resonance components (adapted from Ref. [10]).

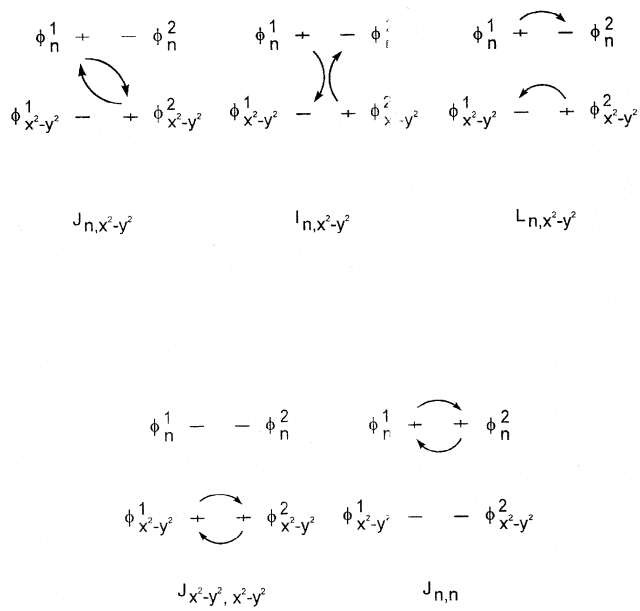

Fig. 6. J, I and L integrals involved in the splitting of LF excited states in the coupled-chromophore model (adapted from Ref. [10]).

allow an estimate of the anisotropic exchange contribution to the ground-state zero-field splitting D.

3. The I integral corresponds to an excitation transfer mediated through the Coulomb interaction [21]. Note that this term involves deexcitation of Cu_A with a simultaneous excitation of Cu_B (Fig. 6). Therefore, this excitation transfer can be estimated by a dipole–dipole approximation involving M, the transition

dipole moment of the absorption band, and geometrical parameters of the complex (transition dipole vector coupling (TDVC)). Using this method, a value of $I_{n,x^2-y^2} = 3\ cm^{-1}$ is obtained for $n = xy$ and z^2; the value for $I_{xz/yz,x^2-y^2}$ is somewhat larger (25 cm^{-1}).

4. The matrix element L corresponds an exchange-mediated excitation transfer [21,22]. In contrast to the Coulomb-mediated transfer, the electrons are exchanged between the centers A and B in this interaction (Fig. 6). It has been shown that the integral L_{n,x^2-y^2} can be written as the square-root of the product $J_{x^2-y^2,x^2-y^2} \cdot J_{n,n}$, which allows one to deduce symmetric coupling constants $J_{n,n}$ from the excited-state L values and the (known) ground-state coupling constant $J_{x^2-y^2,x^2-y^2}$. This provides direct insight into the superexchange pathways between all different combinations of d-orbitals on each copper. Importantly, this evaluation gives a very small coupling constant between the two z^2-orbitals, $J_{z^2,z^2} < 8\ cm^{-1}$, excluding significant metal–metal bonding along the Cu–Cu axis for this dimer. Surprisingly, $-2J_{xz/yz,xz/yz}$ is found to be much larger (1617 cm^{-1}) than $-2J_{x^2-y^2,x^2-y^2}$ (325 cm^{-1}) which might be expected to have the largest $-2J_{n,n}$ value. An explanation for this finding in terms of bridging carboxylate superexchange pathways is given in Ref. [10].

To summarize, the investigation of the $Cu_2(acetate)_4$ system has provided the first detailed and complete information regarding binuclear interactions in the LF excited states of a transition-metal dimer. Since all excited states involve interconfigurational transitions, this picture is more general than the phenomenological description of dimer couplings in spin-flip states of, e.g. Cr(III) and Mn(II) which involve intraconfigurational LF transitions. In the latter case excited-state interactions are—just as for the electronic ground state—described by a Heisenberg Hamiltonian (1) which only involves the (excited-state) coupling parameter J. This approach (Tanabe model) will be further discussed and evaluated in terms of the VBCI model in Section 5. Treatments where, in contrast to the coupled-chromophore model or the Heisenberg (Tanabe) formalism, the mutual overlap of d-orbitals via bridging ligands is explicitly included in the description of LF excited-state splittings will also be discussed in Section 7. However, before proceeding with LF states the interactions present in CT excited states of transition-metal dimers will be presented and their relevance to the magnetic properties of the ground-state considered.

4. Shifts and splittings in CT states of bridged dimers: symmetrically peroxo and azido bridged copper systems, hemocyanin and the VBCI model [15,23,24]

A detailed understanding of the CT spectroscopic features of bridged dimers has been prompted by the effort to understand the characteristic optical absorption and CD spectrum of oxy-Hemocyanin (Fig. 7) [11–13,23]. Hemocyanin (Hc), the oxygen-transport protein of molluscs and arthropods, contains a binuclear Cu(I) active site that reversibly binds dioxygen as peroxide in a side-on bridging (μ-η^2:η^2) fashion (Scheme 3(A)). The same binuclear copper center is contained in the

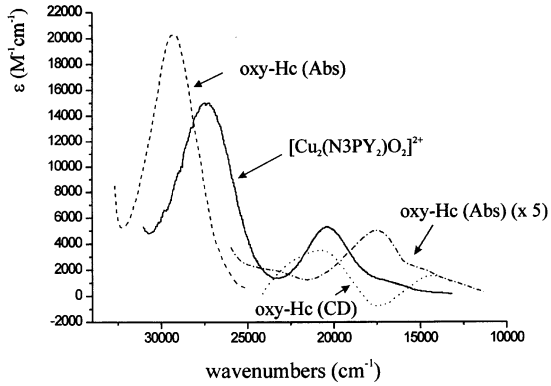

Fig. 7. Optical absorption and CD spectrum of oxy-Hemocyanin and the model complex $[Cu_2(N3PY2)O_2]^{2+}$. While the spectrum of oxy-Hc is typical for μ-η^2:η^2 Cu peroxo systems with an almost planar Cu_2O_2 unit, the model complex has a bent side-on peroxo bridged (butterfly) structure (see text; adapted from Ref. [24]).

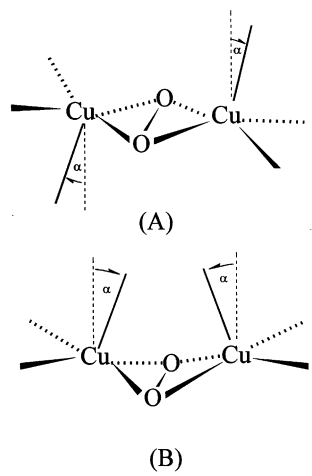

Scheme 3.

enzymes catechol oxidase and tyrosinase mediating the hydroxylation of phenols and the conversion of phenols to *o*-quinones, respectively [13]. One important goal of synthetic, mechanistic, spectroscopic and theoretical efforts related to these coupled binuclear Cu proteins has been to understand how the electronic structure of the binuclear side-on peroxy bridged Cu(II) active site relates to that of other mono- and binuclear Cu systems exhibiting end-on terminal and end-on bridging geometries, respectively, and how it contributes to the reactivity of this site in oxygen metabolism.

The highest occupied molecular orbitals of peroxide are a doubly degenerate π^* set. Upon bonding to a metal center, these orbitals split in energy into a σ-bonding orbital within the plane of the metal-peroxo bond, π^*_σ, and a π-bonding orbital vertical to this plane, π^*_v (Fig. 8). In the UV–vis region of the spectrum, CT transitions from these peroxide orbitals to unoccupied or partly occupied metal orbitals can be observed. In the case of Cu(II) peroxo compounds, $O_2^{2-} \rightarrow$ Cu CT bands are assigned to electronic transitions from the ligand to the singly occupied x^2-y^2 orbital of the metal. As σ- is much stronger than π-bonding, the π^*_σ-orbital is much lower in energy than the π^*_v-orbital, and the $\pi^*_\sigma \rightarrow x^2-y^2$ CT transition is expected to be at much higher energy than the $\pi^*_v \rightarrow x^2-y^2$ transition. From overlap considerations with respect to x^2-y^2, the intensity of the π^*_σ will be much higher than that of the π^*_v transition. In agreement with this bonding description, two peroxide $\rightarrow$ Cu CT transitions are observed in the optical absorption spectrum of a mononuclear, end-on peroxo coordinated copper complex, one high-intensity $\pi^*_\sigma \rightarrow x^2-y^2$ transition at 19 900 cm^{-1} ($\varepsilon = 6300$ M^{-1} cm^{-1}), and one $\pi^*_v \rightarrow x^2-y^2$ transition of lower intensity at 16 600 cm^{-1} ($\varepsilon = 1100$ M^{-1} cm^{-1}) [25a,b]. Alternatively, oxy-Hc exhibits *three* dominant absorption features which have been interpreted as peroxide $\rightarrow$ Cu transitions, two bands in the optical absorption spectrum

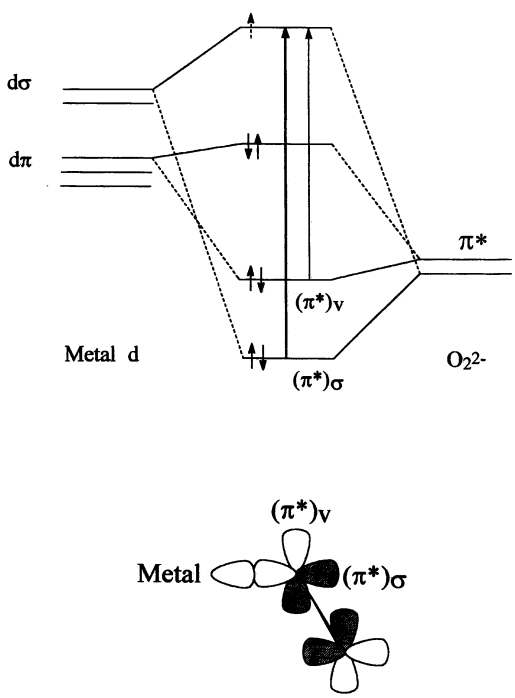

Fig. 8. Molecular orbital diagram (valence orbitals on top) of a monomeric copper peroxo complex. The two possible charge-transfer transitions are indicated, with their relative intensities given by the thickness of the arrow.

at 17 200 ($\varepsilon = 4000$) and 29 000 cm^{-1} ($\varepsilon = 20\,000\ M^{-1}\,cm^{-1}$) and one absorption feature in the CD spectrum near 480 nm ($\Delta\varepsilon = 1\ M^{-1}\,cm^{-1}$) (Fig. 7) [11–13]. This has been taken as evidence that peroxide bridges the two copper centers which is compatible with resonance Raman data that indicate that peroxide is bound symmetrically (i.e. bridging, but not μ-1,1), in agreement with the crystal structure of oxy-Hc [26]. In addition, optical absorption features almost idential to oxy-Hc have been found in a small-molecule binuclear Cu(II) complex, the X-ray structure analysis of which indicated a side-on bridged structure [27,28]. Similar findings have now been obtained for a large number of related systems [29].

Just like in the case of LF transitions, every monomer CT transition corresponds to two CT transitions in the dimer. In general, these two transitions split in energy due to dimer interactions present in the coupled electronic system. The first direct experimental evidence for the dimer splitting of a CT transition has been obtained in a comparative study of mono- and binuclear copper azide systems (Fig. 9) [14]. The HOMO of azide is of non-bonding (nb) type and doubly degenerate. Upon binding to, e.g. Cu(II), it splits into $(\pi^{nb})_\sigma$ and $(\pi^{nb})_v$ in the same way as $\pi^*(O_2^{2-})$; copper azide systems may therefore serve (and in fact have been used) as electronic-structural and spectroscopic analogues of copper dioxygen adducts. In and end-on azide coordinated monomer, the $(\pi^{nb})_\sigma \rightarrow Cu\ x^2 - y^2$ transition is observed at 25 300 cm^{-1} ($\varepsilon = 2000\ M^{-1}\,cm^{-1}$). This transition splits in the binuclear complex

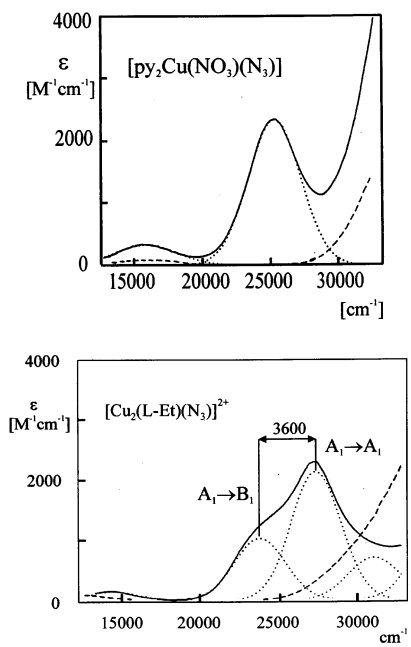

Fig. 9. Optical absorption spectra of the end-on terminally azide-coordinated complex $[py_2Cu(NO_3)(N_3)]$ (a; top) and the *cis* μ-1,3 azide bridged, binuclear Cu complex $[Cu_2(L–Et)(N_3)]^{2+}$ (b; bottom). Note the splitting of the azide→Cu(II) LMCT band in the dimer (see text; adapted from Ref. [30]).

$[Cu_2(L–Et)(N_3)]^{2+}$ into two transitions at 27 400 ($\varepsilon = 2100$) and 23 800 cm^{-1} ($\varepsilon = 1000$ $M^{-1}\,cm^{-1}$). This dimer contains a *cis* μ-1,3 bridging azide ligand between two Cu(II) centers, in addition to a bridging alkoxide group deriving from the binucleating ligand L–Et [14]. The two copper centers are strongly antiferromagnetically coupled ($-2J \geq 1200$ cm^{-1}). Since met-azide Hc gives a nearly identical absorption spectrum, it was concluded that azide is also bound in a *cis* μ-1,3 fashion in the protein [14].

In order to account for the observed spectroscopic data, a TDVC model was applied which relates the dimer splitting to the interaction energy of the transition dipoles at the two monomer subunits (cf. Section 3). From the observed intensity of the azide → Cu CT transition, however, a splitting energy was obtained for the LMCT state which was one order of magnitude smaller than the observed value. In view of this difference, the interactions present in the CT excited electronic states of coupled dimers have been analyzed theoretically considering a Cu(II) dimer bridged by a ligand L [15]. For a treatment of the L → M CT states within a minimal basis, only the highest MO of L being occupied by two electrons and the two electrons in the highest, singly occupied MOs of the Cu(II) centers have been included, containing a total of four electrons. Evaluation of the diagonal energies of the four-electron Hamiltonian

$$H = \sum_{i=1}^{4} h(i) + \sum_{\substack{i,j=1 \\ i<j}}^{4} e^2/r_{ij} \tag{4}$$

using symmetry and spin-adapted wavefunctions gives an energy level scheme that is similar, though not identical to that obtained for the coupled-chromophore, two-hole treatment of the LF states of Cu acetate (cf. Section 3, Fig. 5). In analogy to this case, there exists a total of four CT excited states for each CT state in the monomer, and the shift and splitting of each monomer CT transition can be described in terms of the four parameters of exciton theory, K, J, I and L. The Coulomb integral K accounts for the overall shift of the dimer with respect to the parent monomer CT states, the exchange integral J determines the magnitude of excited-state singlet–triplet splitting, and I and L, the 'Coulomb' and 'exchange mediated excitation transfer' integrals, respectively, are responsible for the 'sym/antisym' splitting of the CT excited states. The contribution to the excited-state splitting due to the I integral corresponds to the value predicted by the coupling of two transition dipoles (TDVC model). However, as indicated above, the singlet CT state splitting observed for $[Cu_2(L–Et)(N_3)]^{2+}$ was found to be an order of magnitude larger than predicted by a TDVC estimate of I and neglect of L (vide infra). In addition, the excited-state exchange integral J is only due to the e^2/r_{12} operator (based on the choice of orthogonalized wavefunctions) and thus positive; this cannot explain the large AF interaction of CT states exhibited by Cu(II) dimers (cf. Section 2). The only integral containing one-electron operators is L; however, decomposition of this integral into two- and one-electron contributions leads to one-electron terms h_{AB} which are small due to the large distance between the Cu centers A and B. From exciton theory, on the other hand, the two-electron part of L is known to be even smaller than I. Therefore, this scheme was found to be

unable to account for the magnitude of CT excited-state splittings observed in binuclear systems.

This finally led to the development of the VBCI model where basically all of the two-electron and diagonal one-electron interactions h_{AB} discussed above are neglected and all dimer splittings are attributed to configuration interaction mediated by a transfer integral β_1 which is proportional to metal–ligand overlap [15].

$$\beta_1 = \langle d_A | h | \pi \rangle = h_{d_A \pi} = \langle d_B | h | \pi \rangle = h_{d_B \pi} \quad (5)$$

Here, d_A and d_B denote the highest occupied d-orbitals of Cu_A and Cu_B, respectively, and π the HOMO of the bridging ligand. We use a dimer symmetry of, e.g. C_{2v} (Fig. 10). In the ground state of the dimer, the two electrons in the Cu orbitals couple to form a $^1A_1$ and a $^3B_1$ state. LMCT transitions can take place to the left Cu (Cu_A) or the right Cu (Cu_B). Linear combinations of these two degenerate, locally excited CT configurations generate two symmetry-adapted CT states, A_1^{CT}

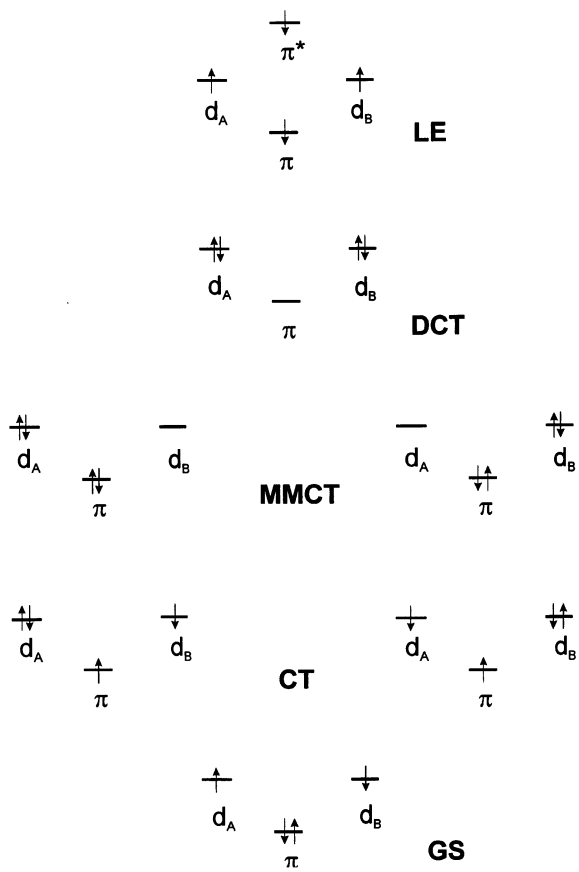

Fig. 10. GS, CT, MMCT, DCT and LE configurations of a Cu(II) dimer bridged by a ligand π-orbital (see text).

and B_1^{CT}. In addition, each CT configuration leaves one unpaired electron in the bridging ligand orbital that couples with the other unpaired electron on a Cu center to a singlet and a triplet state. Taking into account the interaction of GS and CT states of the same symmetry by the matrix element β_1, the energy level scheme of Fig. 11 is obtained. Both singlet and triplet CT states of the dimer split by an amount

$$\delta_1 = \frac{2\beta_1^2}{\Delta} \tag{6}$$

which provides experimental information about the magnitude of the transfer matrix element β_1; Δ is the CT energy. Note that δ_1 also corresponds to the ground-state stabilization; however, at the present level of approximation, *both* singlet and triplet GS components are lowered in energy by δ_1 and are therefore degenerate. Hence, four symmetry-allowed CT transitions are predicted as indicated in the figure, two singlet → singlet and two triplet → triplet transitions. It can be shown that also at this level of approximation the two lower-energy transitions are at the same energy as the CT transition in the monomer [30]. Further, the energies of the two triplet states can equally be determined from MO theory where the splitting between them corresponds to the HOMO–LUMO gap of the complex; this is not true for the singlet CT states.

This model is now applied to the above-mentioned *cis* μ-1,3 azido bridged binuclear complex $[Cu_2(L–Et)(N_3)][BF_4]_2$ [15]. As the triplet ground state is not populated, both CT bands correspond to singlet → singlet CT transitions. In accordance with the prototype energy level scheme (Fig. 11), these transitions appear split. In view of the fact that the triplet CT transitions cannot be observed in this system an estimate of their energies has been obtained by SCF-Xα transition-state calculations. These are indicated on the right half of the energy level scheme in Fig. 12. Obviously, the predicted triplet energies are several thousand cm^{-1} higher than the observed singlet energies, and the calculated triplet CT state splitting is about twice as large as the observed singlet CT state splitting. The first result is consistently found in this type of calculation for bridged dimers and

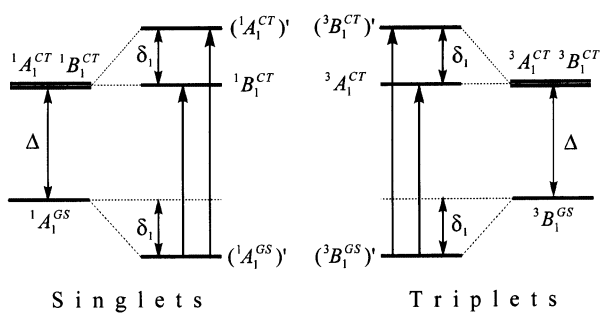

Fig. 11. Energy-level scheme of a binuclear complex (symmetry C_{2v}) along with interaction parameters and optical CT transitions (taken from Ref. [30]).

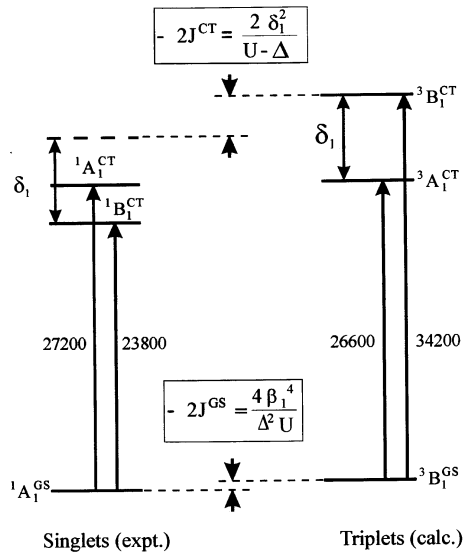

Fig. 12. Energy level scheme with observed and calculated transitions, interaction energies and ground-state/excited-state coupling constants for the binuclear *cis* μ-1,3 azido Cu(II) complex $[Cu_2(L–Et)(N_3)](BF_4)_2$ (adapted from Ref. [30]).

corresponds to the large AF interaction in the CT excited state (ESAF) which lowers the energy of the singlet with respect to the triplet CT states by several 1000 cm^{-1}. This effect cannot be described by MO theory at the Hartree–Fock level and is due to direct overlap between the unpaired electron in a ligand orbital with an unpaired electron in a Cu orbital in the CT excited state (cf. Section 2). In terms of the VB description, this interaction is accounted for by CI with a metal → metal CT (MMCT) state, i.e. a state where one electron has been transferred from one Cu to the other (Fig. 8). The energy of this state is the so-called Mott–Hubbard U for which Cu(II) compounds has been determined to 6.5 eV [31]. The fact that the singlet CT state splitting is smaller in absolute magnitude than the triplet CT state splitting is due to another excited-state interaction which is described in Section 5. Without taking this contribution into account, the $^1A_1^{CT}$ state is lowered with respect to the $^3B_1^{CT}$ state by

$$-2J^{CT} \equiv E[(^3B_1^{CT})'] - E[(^1A_1^{CT})'] = 2\frac{\beta_1^2}{U-\Delta} \tag{7}$$

(the primes denote GS/CT mixed states). As a consequence, the $^1A_1$ ground-state component is lowered with respect to the $^3B_1$ component by

$$-2J^{GS} \equiv E[(^3B_1^{GS})'] - E[(^1A_1^{GS})'] = 4\frac{\beta_1^4}{\Delta^2 U} \cong \lambda^2(-2J^{CT}) \tag{8}$$

the last equality follows from Eq. (7) and $(U-\Delta) \cong U$ (cf. Fig. 12). Hence, the origin of the AF coupling in the ground state is the depression of the $^1A_1^{CT}$ with

respect to the $^3B_1^{CT}$ state, and the corresponding GS coupling constant is given by the excited-state $-2J$ scaled down by the square of the ground-state/CT state mixing coefficient λ,

$$\lambda = -\sqrt{2}\frac{\beta_1}{\Delta} \tag{9}$$

This mechanism of AF coupling is referred to as *superexchange*.

The preceding VBCI analysis has also been applied to the side-on peroxo bridged binuclear Cu(II) site present in oxy-Hc [23]. The π_σ^*-orbital is the dominant bridging orbital of peroxide. The active site of oxy-Hc was modeled using a simplified $[(NH_3)_4Cu_2(O_2)]^{2+}$ planar core (symmetry D_{2h}) [32], and the relative energies of the MO triplet states were determined with SCF-Xα-SW transition-state calculations (see above). These energies were related to VBCI parameters — the zeroth-order energies for the π_σ^* CT ($\Delta\sigma$) and the π_ν^* CT (Δ_ν) states as well as the magnitude of the transfer element $(h_{d\pi})_\sigma$. The zeroth-order energy for the MMCT state was assumed to be equal to the Mott–Hubbard energy U (vide supra). In addition, the VBCI scheme was complemented by a CT state involving transfer of the two electrons in π_σ^* to the two Cu(II) centers (DCT state; E_{DCT}); this appears to be necessary whenever the bridging ligand is able to donate two electrons to the metal centers (Fig. 10). In D_{2h} symmetry the π_ν^*-orbital has no overlap with the Cu x^2-y^2 orbitals, and hence $(h_{d\pi})_\nu = 0$. However, including the *trans*-axial ligands lowers the dimer symmetry to C_{2h}, and due to the pyramidal coordination, the quantization axis of each copper center is tilted with respect to the Cu_2O_2 plane (Scheme 3(A)). Therefore, the matrix element $(h_{d\pi})_\nu$ becomes non-zero; its value was estimated from the relative, experimentally determined oscillator strengths of the π_σ^* and π_ν^* absorption bands. Using the VBCI parameters obtained this way, the A_g component of the $\pi_\sigma^* \rightarrow$ Cu(II) CT transition (electric-dipole forbidden) was calculated to be ca. 2000 cm^{-1} above the electric-dipole allowed B_u component (observed experimentally at 345 nm), and the splitting of the two components of the $\pi_\nu^* \rightarrow$ Cu(II) transition was calculated to be ≈ 3000 cm^{-1} with the CD-active band (A_g component) being above the electric-dipole allowed band (B_u component), in agreement with the experimental observations (Fig. 13, left).

More recently Pidcock et al. extended the above treatment to Cu_2O_2 cores that exhibit a butterfly structure, i.e. bent around the O–O axis (Scheme 3(B)) [24]. Absorption spectra of these systems have revealed one additional intense band around 420–490 nm as compared to the planar Cu_2O_2 cores (Fig. 7). Spectroscopic analysis shows that this band is one component of the $\pi_\sigma^* \rightarrow$ Cu(II) transition which becomes allowed in the lower symmetry of the bent geometry. To apply the VBCI model to the C_{2v} butterfly core, values for Δ_σ, $(h_{d\pi})_\sigma$, Δ_ν and $(h_{d\pi})_\nu$ were determined based on triplet CT transition-state calculations. Note that like in the C_{2h} case (vide supra), non-vanishing values of $(h_{d\pi})_\nu$ are due to a rotation of the Cu quantization axes caused by bending of the O_2CuN_2 units around the common O–O axis (Scheme 3(B)). From DFT calculations based on this distorted geometry, the values of Δ_σ and $(h_{d\pi})_\sigma$ are found to have decreased from those calculated for the planar C_{2h} model, reflecting the loss of interaction between the peroxide π_σ^* and the Cu

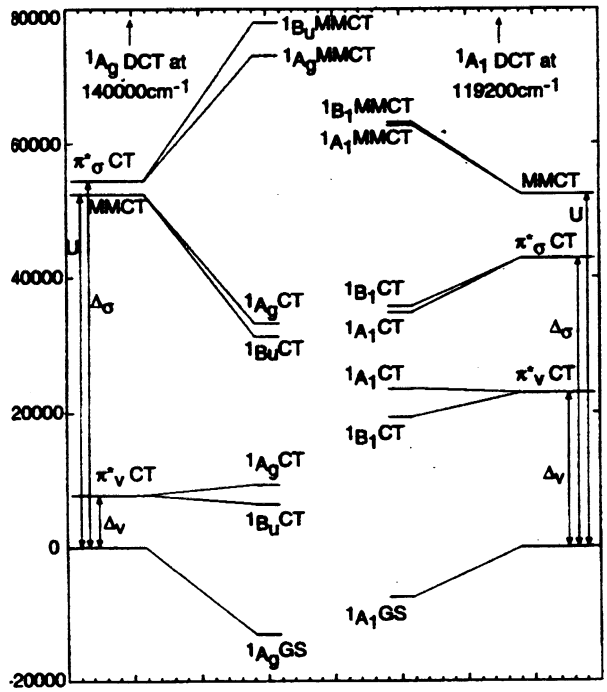

Fig. 13. VBCI diagram for a side-on peroxide-bridged copper dimer in planar (left) and butterfly (right) geometries. Unperturbed singlet states are shown for both planar and butterfly geometries (far left and far right, respectively) and after CI is introduced between the GS, CT, and higher energy CT states (MMCT and DCT, DCT omitted from diagram for clarity) (center left, planar; center right, butterfly). Taken from Ref. [24].

x^2-y^2 orbitals in the butterfly core. In contrast, due to the greater interaction between the peroxide π^*_v and the Cu x^2-y^2 orbitals, the magnitude of the zeroth-order energy Δ_v and the transfer matrix element $(h_d\pi)_v$ have increased compared with those of the planar core. Diagonalization of the VBCI matrices using these parameters gives the energies for the π^*_σ and π^*_v CT states as shown in Fig. 13, right. Importantly, the A_1 component of the π^*_σ CT is now calculated to be ca. 900 cm^{-1} *below* the B_1 component, in contrast to the results obtained for oxy-Hc (C_{2h}), where the A_g component of the π^*_σ CT was calculated to be ca. 2000 cm^{-1} *above* the B_u component. This order of π^*_σ CT state components is in qualitative agreement with the experimental observation. Further, the splitting between the two components of the π^*_v CT state is calculated to be ca. 4000 cm^{-1}, compared with the splitting of ca. 2900 cm^{-1} calculated for the planar C_{2h} core. This is in good agreement with the spectroscopic data which show the splitting of the π^*_v states to be ca. 5000–6000 cm^{-1}, compared with the ca. 3000 cm^{-1} splitting in oxy-Hc.

Thus the VBCI model gives a satisfactory account of the peroxo → Cu transitions in side-on coordinated Cu(II) systems exhibiting a planar Cu_2O_2 core, including oxy-Hc, and reproduces the lower energy A_1 component of the π^*_σ CT transition and the larger splitting of the π^*_ν CT transition observed experimentally for the butterfly core. These spectral changes are due to a reduced interaction of the Cu x^2-y^2 orbitals and the peroxide π^*_σ-orbital and the significantly increased interaction of the Cu x^2-y^2 orbitals with the peroxide π^*_ν-orbital, as also observed in electronic-structure calculations [24].

5. Excited-state ferromagnetic coupling: the case of ferromagnetically coupled Cu(II) azido dimers [30,33]

Having determined how the AF interaction in the CT excited state (ESAF) present in the *cis* μ-1,3 azido and side-on peroxo bridged Cu(II) dimers gives rise to a strong AF contribution to the ground-state magnetic coupling constant $-2J$ (Eq. (8)), it was of interest to look for a similar *ferromagnetic* interaction in the CT state (ESF) which would be responsible for the strong ferromagnetic coupling present in the ground state of μ-1,1 azido bridged Cu(II) dimers. More specifically, an orbital mechanism had to be identified which would overcome the dominant AF MMCT pathway always present in bridged dimers, thus leading to a net ferromagnetically coupled ground state. This has been achieved by taking into account the LUMO of the bridging ligand, i.e. in case of azide the π*-orbital at an energy of ca. 3 eV above the HOMO (π^{nb}) [30,33].

The GS, CT, MMCT and DCT configurations and states as well as their interactions have been described in Section 4. The new configuration coming into play by taking the π*-orbital into account is the 'ligand excited' (LE) configuration which can be reached from the CT configuration by shifting one electron from the doubly occupied Cu orbital to π* (Fig. 9). In this LE configuration, there are four unpaired electrons occupying the set of four orbitals. The corresponding LE states can be considered as arising from a coupling between a singlet or a triplet configuration of the metal centers with a ligand localized excited ($\pi^{nb}\pi^*$) singlet or triplet state. Thus, the metal singlet ($S=0$) can couple with a ligand excited singlet ($S=0$) to a singlet ($S=0$) and with a ligand excited triplet ($S=1$) to produce a triplet ($S=1$). The metal triplet can couple with a ligand excited singlet to a triplet ($S=1$) and with a ligand excited triplet to form a quartet, triplet and singlet state ($S=2,1,0$). Hence, there are in total one quartet, two triplets and two singlets. The LE states arising from a coupling between the metal triplet and the excited ligand triplet are denoted by a subscript t.

In zeroth order, all CT states are at the same energy Δ, the MMCT states are at an energy U and all LE states are at an energy $\langle\pi^*\rangle$ above the ground state. In Section 4, the shifts and splittings of the CT states have been induced by the off-diagonal element β_1 (5) of the one-electron part of Eq. (4). Now, we consider in addition the off-diagonal matrix element

$$\beta_2 = \langle d_A | h | \pi^* \rangle = \langle d_B | h | \pi^* \rangle \quad (10)$$

representing a transfer of an electron from the copper d-orbitals to the azide π*-orbital. The new interaction CT–LE is shown in Fig. 14 which displays the energy levels of the CT and LE states before (i.e. at zeroth-order) and including the CT–LE off-diagonal matrix elements, respectively, in a perturbation limit ($\beta_2 \ll [\langle \pi^* \rangle - \Delta]$). The calculation shows that, for the μ-1,1 azide systems, the CT–LE interaction acts to lower both singlet and triplet A_1^{CT} and B_1^{CT} states, but the B_1 states three times more than the A_1^{CT} states (triplets as well as singlets). In particular, the $^3B_1^{CT}$ state is lowered with respect to the $^3A_1^{CT}$ state. This is the mechanism of ferromagnetic interaction in the CT excited state of μ-1,1 azide bridged dimers mediated by the π*-orbital (ESF). Further, it is seen that the major part of this selective lowering of the B_1^{CT} states results from a coupling between the metal triplet and excited ligand triplet in the $_tB_1^{LE}$ state. Since the triplet ground-state component has B_1 and the singlet component A_1 symmetry, the lowering of $^3B_1^{CT}$ acts to shift $^3B_1^{GS}$ below $^1A_1^{GS}$ corresponding to the observed ferromagnetic coupling in the ground state.

For the *cis* μ-1,3 azide systems (not shown) calculation shows that the CT–LE interaction lowers the A_1^{CT} states three times stronger than the B_1^{CT} states (triplets as well as singlets). In particular, the $^1A_1^{CT}$ state is lowered with respect to the $^3B_1^{CT}$ state. This corresponds to an AF interaction in the CT excited state of cis μ-1,3 azide bridged dimers mediated by the π*-orbital which complements the AF contributions due to MMCT and DCT states described in Section 4, Fig. 12. Again, the major part of this selective lowering of the A_1^{CT} states is due to interaction with the $_tA_1^{LE}$ states, i.e. the A_1^{LE} states resulting from a coupling between the metal triplet and excited ligand triplet.

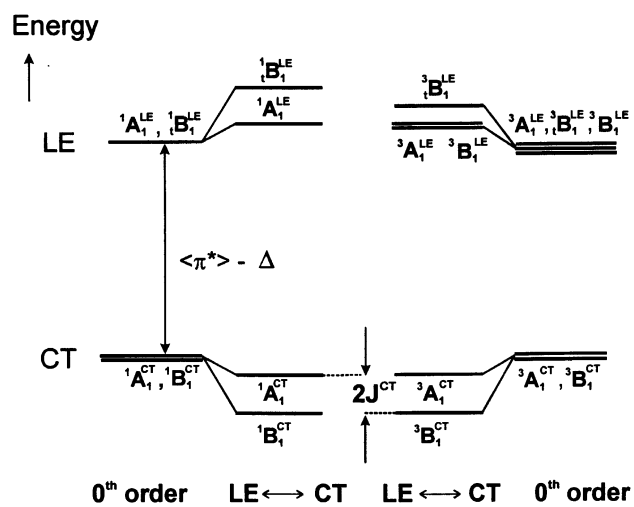

Fig. 14. VBCI interaction scheme between the CT and LE states of a μ-1,1 azido Cu(II) dimer. Note the position of $^3B_1^{CT}$ which is lower than $^1A_1^{CT}$ corresponding to a CT excited ferromagnetic coupling ($2J^{CT} > 0$).

Thus, the case of *cis* μ-1,3 and μ-1,1 azido bridged Cu(II) dimers has shown that for a detailed understanding of the magnetic properties of the ground state, inclusion of the bridging ligand LUMO may also be important. This can alternatively be demonstrated in terms of a MO analysis of the respective ground states showing that in case of the μ-1,1 azido dimers the HOMO and the LUMO of the bridging azide have opposite effects on the HOMO–LUMO splitting of the complex, whereas in the case of the *cis* μ-1,3 dimers both the HOMO and the LUMO of the bridging azide act to increase the HOMO–LUMO splitting of the complex [33]. In the framework of the VBCI model, the ($\pi^{nb}\pi^*$) ligand excited states mediate a powerful ferromagnetic interaction provided the symmetry of these orbitals is such that the triplet ground-state component is selectively lowered in energy. In this case the ubiquitous AF term due to MMCT can be suppressed leading to net ferromagnetic coupling in the electronic ground state. Importantly, the corresponding excited-state ferromagnetic interaction (ESF) has been evidenced by optical absorption spectroscopy of mono- and bis μ-1,1 azido Cu(II) dimers [33].

6. Exchange effects in LF states (B) — strong coupling in spin-flip states: VBCI-evaluation of excited-state *J*s [9]

Traditionally, spin-forbidden excitations within the ground electron configuration have been a domain of the optical-spectroscopic determination of excited-state exchange interactions since these transitions often consist of sharp lines and thus can be very informative. Of particular interest in this connection have been the $^4A_2 \rightarrow {}^2E$ and $^4A_2 \rightarrow {}^2T_1$ transitions of Cr^{3+} which, in a dimer, give rise to the 'singly excited' (SE) $^2E^4A_2$ and $^2T_1^4A_2$ pair states where one metal center is in the excited state and the other one is in the ground state. The exchange splittings of the $^4A_2^4A_2$ ground and $^2E^4A_2$ as well as $^2T_1^4A_2$ and $^2T_2^4A_2$ SE states were investigated for a number of mono-, di- and tri-μ-hydroxo bridged chromium(III) dimers [9]. The observed energy splittings were described by the phenomenological Heisenberg Hamiltonian (1), using exchange parameters J_i that were determined for the ground state and excited states i separately (Tanabe model). Importantly, exchange parameters derived from SE state splittings were found to be about 25–100% larger than for the ground state, indicating an increase of the exchange interaction with increasing energy. This behavior was found to be typical for exchange-coupled systems, but had not been reproduced by theory. By investigating the tri-μ-hydroxo bridged Cr(III) dimer $[Cr_2(OH)_3(tmtame)_2]^{3+}$ (**1**), Schenker et al. showed that (i) the VBCI model can be applied to determine excited-state 2*J*s for spin-flip excited states of, e.g. Cr(III) dimers just as for the magnetic coupling constant of the ground state, and (ii) that the VBCI model allows an understanding of both the ground and the excited-state 2*J*s with one set of parameters. Therefore, the VBCI model provides a natural explanation for the observed increase in magnitude of excited state 2*J*s with respect to the ground-state value [9].

In this system the region of single excitations (SEs) extends from about 15 000–25 000 cm^{-1} and is partly masked by intense, spin-allowed LF transitions ($^4T_2$,

$^4T_1$), whereas the double excitations (SPEs) range from 27 000 to about 40 000 cm^{-1}. Detailed information regarding excited-state interaction can mostly be derived from the SE states while definite assignments in the SPE region are more difficult. In order to interpret the experimental results, the VBCI model has been adapted to include the three configurations 'ground' (GR) $(t_2^3)_A L^N (t_2^3)_B$; 'LMCT' $(t_2^4)_A L^{N-1} (t_2^3)_B / (t_2^3)_A L^{N-1} (t_2^4)_B$; and 'MMCT' $(t_2^2)_A L^N (t_2^4)_B / (t_2^4)_A L^N (t_2^2)^B$. Note that $(t_2)^3$ refers to the ground-state configuration on Cr(III) center A and B with three electrons of parallel spin in the set of three t_2-orbitals whereas L^N corresponds to the set of three closed-shell bridging ligands (3 OH^-) with N electrons in total. In addition to the LM- and MMCT energies Δ and U, respectively, the single-ion energies for the octahedral LF states ^2E, $^2T_1$ and $^2T_2$ are required. Moreover, the approximate C_{3v} symmetry of the Cr^{3+} ion site splits the set of t_2-orbitals by δt_2 into two sets of orbitals with a_1 and e symmetry.

According to Fig. 15 two types of interaction are considered: a direct interaction between the orbitals centered on the metals A and B (direct exchange), and an indirect interaction involving ligand orbitals (superexchange). Direct interaction between $(a_1)_A$, $(a_1)_B$ or $(e)_A$, $(e)_B$ will result in the following non-zero matrix elements, respectively:

$$h_{\pi MM} = \langle (a_1)_A | h | (a_1)_B \rangle \tag{11a}$$

$$h_{\pi MM} = \langle (e_x)_A | h | (e_x)_B \rangle = \langle (e_y)_A | h | (e_y)_B \rangle \tag{11b}$$

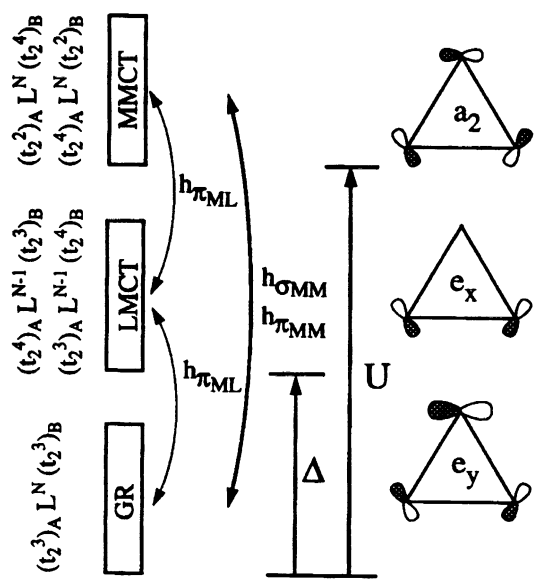

Fig. 15. Schematic representation of the model parameters used to describe the optical spectrum of $[Cr_2(OH)_3(tmtame)_2]^{3+}$. The ground, LMCT, and MMCT electron configurations are shown on the left. The ligand orbitals lying in the plane formed by the three oxygen atoms are shown on the right. Taken from Ref. [9].

For the indirect interaction, only the highest-energy ligand orbitals having π-symmetry are considered. These all lie in a plane defined by the three oxygens and transform as a_2 and e, respectively, in the ca. C_{3v} single-ion frame. The only symmetry-allowed M–L interaction is thus of e-type, and the corresponding one-electron transfer element is defined as

$$h_{\pi ML} = \langle (e_x)_A | h | (e_x)_L \rangle = \langle (e_y)_A (e_y)_L \rangle \quad (12)$$

A total of 834 pair functions comprising all electronic states resulting from the GR configuration as well as those deriving from the LMCT and MMCT configurations have been used in the calculations. Ground and excited-state exchange interactions arise from the mixing induced by the parameters $h_{\sigma MM}$, $h_{\pi MM}$ and $h_{\pi ML}$ where $h_{\pi ML}$ couples GR with LMCT states and LMCT with MMCT states and $h_{\sigma MM}/h_{\pi MM}$ couple GR with MMCT states. An energy level scheme resulting from a fit of the experimentally determined SE levels is given in Fig. 16 showing good agreement. The corresponding electron-transfer parameters are given as $h_{\sigma MM} = -5723\ cm^{-1}$, $h_{\pi MM} = -2366\ cm^{-1}$ and $h_{\pi ML} = -3905\ cm^{-1}$. Thus, the direct

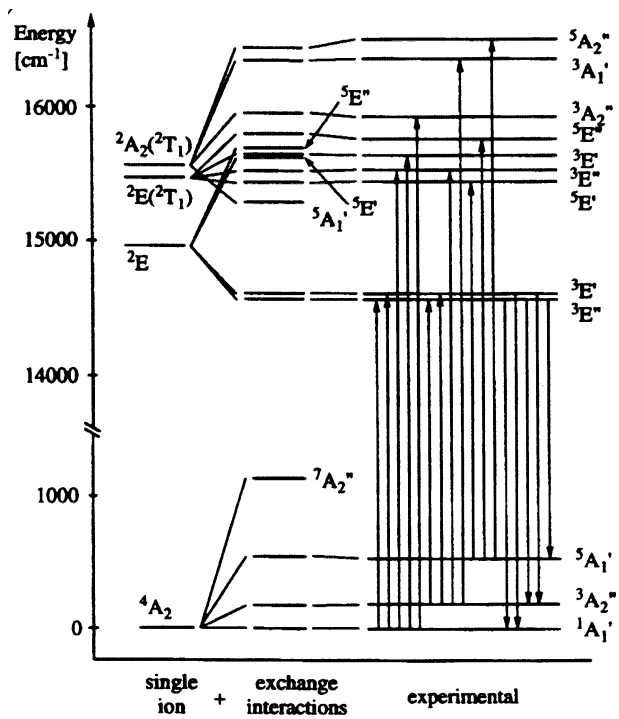

Fig. 16. Energy level diagram of the $^2E^4A_2$, $^2T_1^4A_2$ singly excited states of $[Cr_2(OH)_3(tmtame)_2]^{3+}$. On the left are the single-ion energy levels in the absence of exchange interactions. In the middle row the interactions represented by the one-electron parameters $h_{\sigma MM}$, $h_{\pi MM}$ and $h_{\pi ML}$ are switched on. On the right the experimental values are shown. The dimer levels are labeled in the approximate D_{3h} symmetry. Taken from Ref. [9].

interaction between the two metal-type a_1-orbitals was shown to be the dominant exchange pathway in these systems. As a consequence, the coupling in the LMCT states was found to be ferromagnetic: transfer of one electron from the ligands to one metal center leads to a situation where the two local CT states can directly interact via $h_{\sigma MM}$. In analogy to double-exchange, the result is a spin-dependent electron transfer between the metal centers which favors ferromagnetic coupling in the CT excited state. Interestingly, the value of $h_{\sigma MM}$ is very close to the value of $|h_{\sigma MM}| = 5516–6538$ cm^{-1} reported for the mixed-valent system $[Fe_2(OH)_3(tmtacn)_2]^{2+}$ [34], showing the close analogy between superexchange mechanism and ET pathway in the analogous one-electron reduced system (cf. Section 8).

7. Exchange effects in LF states (C) — interconfigurational transitions, strong coupling and mixed interactions: iron- and manganese-oxo dimers [7,12,16]

Binuclear mono-oxo bridged $Mn(III)_2$ and $Fe(III)_2$ complexes have been intensively studied because of their relevance to metalloprotein active sites. It has been found that the ground-state magnetic coupling constant J strongly depends on the metal ions and the bridging angle: while the Mn(III) centers in $[Mn(III)_2O(OAc)_2(Me_3tacn)_2]^{2+}$ (**1**; Mn–O–Mn angle = 121°) are weakly ferromagnetically coupled ($J = +9$ cm^{-1}), the Fe(III) centers in the analogous iron complex exhibit strong AF coupling, $J = -119$ cm^{-1}. In addition, the nature of the magnetic exchange interaction in oxo-bridged Mn(III) dimers strongly depends on the bridging angle, changing from strongly AF in a nearly linear complex, $J = -120$ cm^{-1}, to essentially uncoupled in bent complexes, while oxo-bridged Fe(III) dimers generally exhibit strong AF coupling with a minor dependence on the Fe–O–Fe angle. This section considers both Mn(III)–O–Mn(III) and Fe(III)–O–Fe(III) dimers and describes the application of the VBCI model to the determination of their electronic structures.

7.1. Mn(III)–O–Mn(III)

In order to experimentally probe the efficiency of individual superexchange pathways in homobinuclear, bent metal-oxo dimers, Brunold et al. investigated **1**

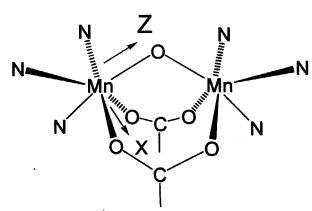

Scheme 4.

(Scheme 4) by variable-temperature single-crystal polarized absorption spectroscopy [16]. Unlike their Fe(III) d^5 h.s. analogs, Mn(III) d^4 h.s. complexes exhibit four spin-allowed LF transitions that involve excitation of an electron from one of the four half-occupied d-orbitals to the single unoccupied orbital which in the present system (C_s monomer symmetry) corresponds to z^2 (z along the Mn–O bond). By comparison with a d^5 $S = 5/2$ half-occupied d-shell, the ground state of each high-spin Mn(III) site can be considered as a z^2 hole state; excited hole states are (in the order of increasing energy) xy, yz, xz and $x^2 - y^2$ (cf. Fig. 17; note that xy and $x^2 - y^2$ have been interchanged due to the choice of the coordinate system). Like in Cu acetate, the ($S = 2$) monomer states are coupled to sym/antisym combinations in the binuclear system (transforming as $^5A_1$, $^5B_1$, $^5A_2$ and $^5B_2$, respectively, in the C_{2v} dimer symmetry) which are split by I and L, the Coulomb and exchange mediated excitation transfer integrals (Fig. 17, center). Further, magnetic coupling with the Mn(III) center left in the ground state ($S = 2$) leads to total spins of $S = 4$, 3, 2, 1 and 0 for each of the SE dimer states (Fig. 17, right). On the other hand, the z^2 $S = 2$ ground states of the two Mn(III) centers give rise to a total spin ladder $S = 4,\ldots,0$. Since the coupling is weak and ferromagnetic (vide supra), the nonet $^9A_1$ lies lowest, but the higher-energy, lower spin quantum numbers are thermally accessible. Fig. 17 includes the observed states with theoret-

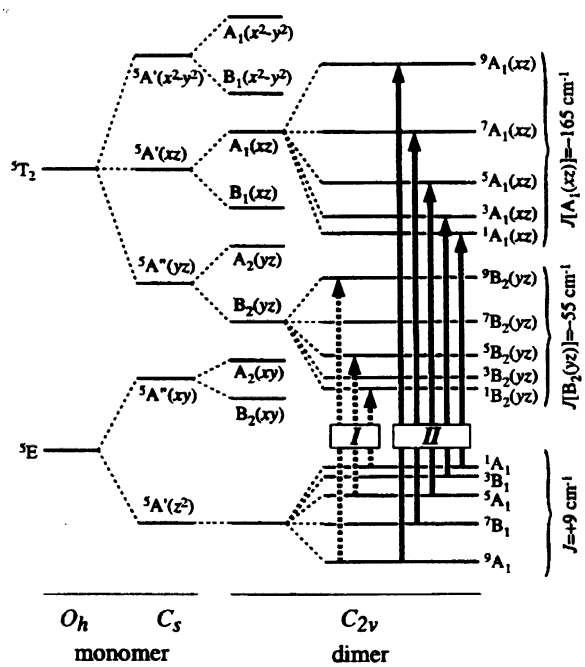

Fig. 17. Schematic energy level diagram for the quintet ligand field (LF) states of Mn(III) in **1** illustrating the effects of the $O_h \rightarrow C_s$ symmetry reduction and dimer formation. The electric-dipole allowed transitions in the C_{2v} dimer symmetry corresponding to bands I and II are indicated by arrows: dotted lines for $E \| y$ and solid lines for $E \perp y$. Taken from Ref. [16].

ically assigned LF transitions which are spin- and electric-dipole allowed based on dimer selection rules. Note that these transitions can be grouped into two regimes, the transitions from z^2 to $B_2(yz)$ (band I) and from z^2 to $A_1(xz)$ (band II).

The optical absorption and MCD spectra showing these transitions are given in Fig. 18. Variable-temperature data reveal that that coupling in both yz and xz excited states is AF ($J = -55\ cm^{-1}$ for $B_2(yz)$ and $J = -165\ cm^{-1}$ for $A_1(xz)$), in contrast to the ground state which is ferromagnetic. This has been rationalized based on Fig. 19. Note that dashed arrows indicate ferro- and solid arrows AF interactions, the coupling strength being indicated by the thickness of the line. The weakly ferromagnetic interaction in the ground state results from a competition between a strongly ferromagnetic interaction being mediated by a 'mixed' $xz \rightarrow z^2$ pathway (vide infra) and two (symmetric) AF pathways, a strong $yz \rightarrow yz$ and a weaker $xz \rightarrow xz$ one (cf. Fig. 20). Note that the ferromagnetic interaction results from two overlapping orbitals (xz on B and z^2 on A or vice versa) sharing a single electron, is of π/σ type and becomes allowed for the bent Mn–O–Mn structure ($\angle$(Mn–O–Mn)ca.120°). In the excited state, one mixed $xz \rightarrow z^2$ pathway turns into an AF one, as it now involves two unpaired electrons in two overlapping orbitals

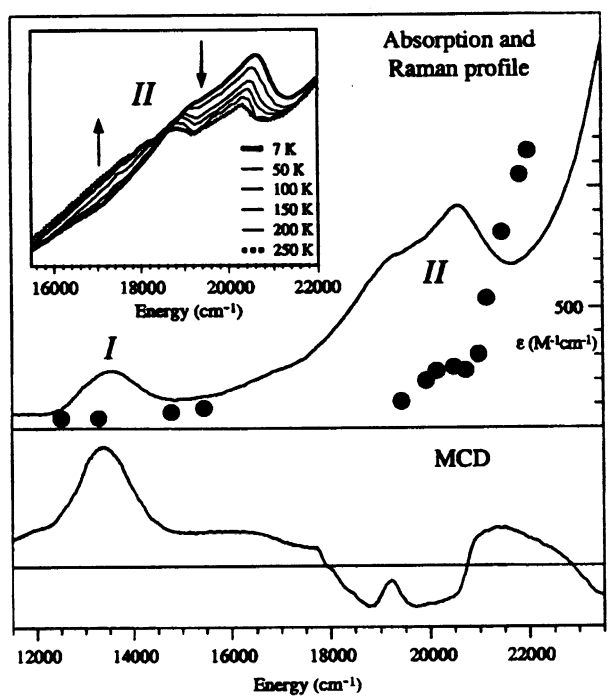

Fig. 18. Solid-state mull absorption (5 K) and MCD (4.5 K, 5.5 T) spectra of **1** in the region of bands I and II (see text). The ~120 K resonance Raman excitation profile for the symmetric Mn–O stretching mode (●) is superimposed on the absorption spectrum. Inset: T dependence of band II (taken from Ref. [16]).

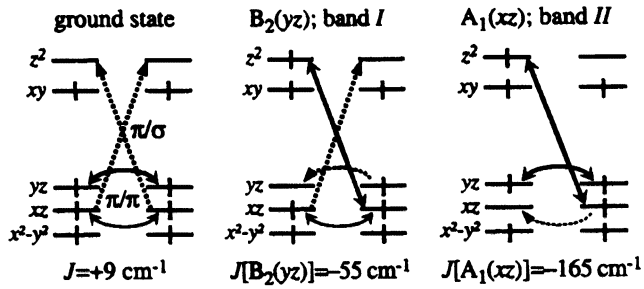

Fig. 19. Schematic illustration of the dominant superexchange pathways in the ground state and the LF excited states corresponding to bands I and II of **1**. Ferromagnetic and antiferromagnetic pathways are indicated by dotted and solid lines, respectively (taken from Ref. [16]).

(cf. Section 2). Further, the symmetries yz–yz pathway in the excited state mediates a ferromagnetic interaction as it involves two overlapping orbitals being occupied by one unpaired electron. In total, this situation leads to a net AF coupling in the yz excited state. In the xz excited state, on the other hand, two strongly AF pathways exist, the mixed xz–z^2 and the symmetric yz–yz one, and only one (weakly) ferromagnetic path, xz–xz (one electron shared), such that the strongest AF coupling is observed.

In order to elucidate the origin of the ferromagnetic coupling in the ground state, the VBCI model was applied to **1**, again including GS, LMCT and MMCT configurations and states. An estimate of the total ground-state splitting $E(S=0)-E(S=4)\equiv 20\ J$ can be obtained from the $S=0$ and $S=4$ VBCI matrices, taking the difference of the respective ground-state energies resulting from diagonalization. Note that starting from the $S=0$ (AF coupled) $^1A_1$ ground-state component, $S=0$ $^1A_1$ MMCT states are reached via $^1A_1$ CT states having Mn(II) $S=3/2$–Mn(III) $S=2$ centers, while starting from the high-spin $S=4$ (ferro) coupled $^9A_1$ GS component, the $S=4$ $^9A_1$ MMCT state is reached via $^9A_1$ CT states having Mn(II) $S=5/2$–Mn(III) $S=2$ centers. The experimental result that in the ground state the $S=4$ is below the $S=0$ component, in spite of a much larger number of AF interactions, is ascribed to the fact that the intervening high-spin $^9A_1$ LMCT states are lowered by about 25 000 cm^{-1} with respect to the $S=0$ $^1A_1$ LMCT states involved in the singlet pathway. This energy corresponds to the spin-flip energy of a mononuclear Mn(II) center ($S=5/2\rightarrow S=3/2$). Importantly, this is still another mechanism which gives rise to an effective ferromagnetic coupling in the CT excited state (cf. Sections 5 and 6) which, in turn, is transferred into the ground state. Moreover, the metal–ligand transfer matrix elements h_{ML} being involved in the mixed interaction leading to ferromagnetic coupling in the ground state are equally responsible for the dominant AF interaction in the LF excited states. Finally, this exchange path is identical to the electron transfer pathway in the one-electron reduced species (cf. next section).

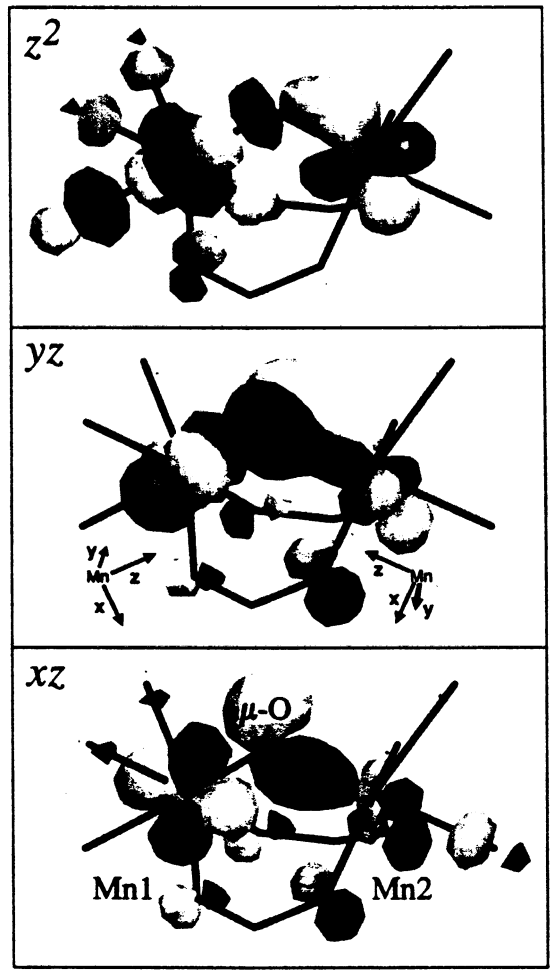

Fig. 20. Boundary surface plots of the Mn1 d-based occupied *xz*, *yz*, and unoccupied z^2 spin-up MOs obtained from a BS calculation on **1** (taken from Ref. [16]).

7.2. Fe(III)–O–Fe(III)

A similar protocol has been applied by Brown et al. to the structurally related, binuclear μ-oxo bis(μ-acetato) Fe(III) complex $[Fe(III)_2O(OAc)_2(Me_3tacn)_2]$ (**2**) serving as a small-molecule model for the active center of met-hemerythrin (met-Hr) [7,12]. The room-temperature and low-temperature glass spectra of **2** shown in Fig. 21 are very similar to those of met-Hr and have been divided into three regions. Note that features in region II are resolved into a number of components which show a striking temperature dependence. Due to magnetic coupling of the two $S = 5/2$ subunits, the ground state of 2 splits into six components giving

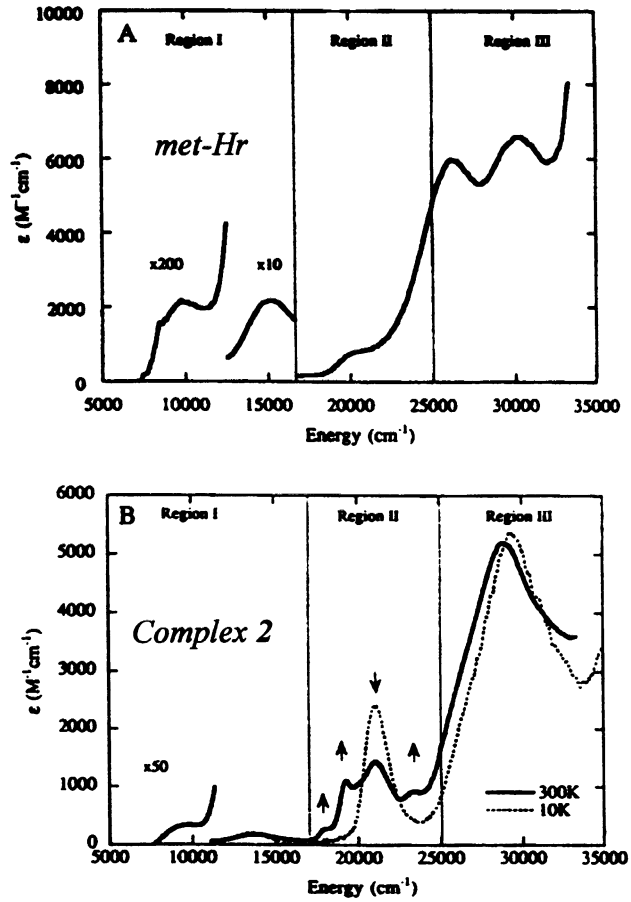

Fig. 21. (Top) Room-temperature absorption spectrum of metCl-Hemerythrin and (bottom) room-temperature and low-temperature (10 K, dotted) absorption spectra of the corresponding model-complex **2** (taken from Ref. [12]).

$S = 0,1,\ldots,5$. With a J^{GS} of -120 cm^{-1}, only the singlet, triplet and quintet sublevels become thermally accessible. The $^6A_1 \rightarrow {}^4\Gamma$ ($\Gamma = T_1$, T_2, A_1/E) LF transitions are spin-forbidden in the monomer, but become allowed in the dimer due to coupling of a locally excited $^4\Gamma$ state with a $^6A_1$ ground state on the other iron center. This gives rise to $S = 1$, 2, 3, 4 LF excited states which in turn are split into 'sym/antisym' combinations due to the I and L integrals (vide supra). As discussed in Section 7.1, a similar interaction occurs for the CT transitions yielding a manifold of total spin CT excited states. In contrast to the LF excited states, spin coupling in the CT states gives the same total spin values as in the GS, i.e. $S = 0,1,\ldots,5$; again, these states are split into sym/antisym combinations. With significant excited-state antiferromagnetism of the oxo $\rightarrow$ Fe(III) CT transitions, the

singlet CT transitions will be stabilized in energy and thus become accessible in the UV–vis spectrum.

Region I of the spectrum contains the dimer transitions originating from the monomer $^6A_1 \rightarrow {}^4T_1$ and $^6A_1 \rightarrow {}^4T_2$ LF bands. These lowest-energy LF transitions of the Fe(III)–O–Fe(III) moiety exhibit several interesting features: first, the intensity of these transitions is at least one order of magnitude greater than what is normally found for Fe(III) monomer transitions. Also, the $^4T_2$ transition is about 20 times more intense than the $^6A_1 \rightarrow {}^4T_1$ transition. In both cases, almost all of the intensity is polarized along the Fe–Fe vector. Finally, the intensity of the $^4T_1$ transition increases by a factor of two with increasing temperature while the $^4T_2$ band exhibits less temperature dependence. These results have been discussed in terms of intensity mechanisms that can be effective for electronic transitions in dimers. The first mechanism involves thermal population of higher spin components of the ground state which then undergo spin-allowed transitions. However, as no $S = 0$ LF excited-state counterpart for the $S = 0$ ground-state component is available (vide supra), this mechanism cannot account for the high absorption intensity observed at low temperature. Therefore, an alternative mechanism must be operative which involves spin–orbit (SO) coupling that overcomes the spin-forbiddeness and is generally present for monomers with spin-selection rules $\Delta S = 0, \pm 1$. The fact that the intensity due to this mechanism increases by an order of magnitude upon going from the monomer to the Fe–O–Fe dimer results from the highly covalent oxo–Fe(III) bond which provides low-energy CT transitions and allows for significant mixing of Fe and oxo centers, making SO coupling of these CT transitions into the LF states more efficient. The intensity increase observed with increasing temperature is ascribed to spin-allowed triplet transitions resulting from the exchange interaction. This mechanism also allows for the observed polarization.

A number of states contribute to the absorption spectrum of **2** in region II. By using a combination of orientationally averaged and polarized absorption, VTMCD, and VT resonance Raman spectroscopies, this region has been assigned as LF and oxo $\rightarrow$ Fe(III) CT transitions. The most intense band at 20 500 cm^{-1} which is assigned to an oxo $\rightarrow Fe^{3+}$ CT transition is a singlet $\rightarrow$ singlet transition which follows from the temperature dependence expected for depopulation of the $S = 0$ component of the ground state. The LF transitions, on the other hand, present evidence of ferro- and AF interactions in the $^4A_1$ and $^4T_2^b$ excited states of the dimer, respectively. On the basis of an analysis for the $^4A_1$ transitions, the mixed π/σ pathways are experimentally determined to be particularly efficient for exchange coupling both in the ground and LF excited states (vide supra).

Region III has been found to contain a number of oxo $\rightarrow$ Fe(III) CT bands which have been analyzed with the help of BS-SCF-Xα calculations and the VBCI model [7,12]. As described in Sections 2 and 4, VBCI explains the large energetic lowering of CT excited states due to overlap between singly occupied ligand and metal orbitals (ESAF). Thus, the lowest-energy CT transition at 20 500 cm^{-1} is assigned to the in-plane (Fe–O–Fe $\equiv$ *yz* plane) oxo $p_y \rightarrow$ Fe *yz* transition, this CT state being subject to the largest excited-state exchange which is the origin of its low energy. The corresponding triplet transition is to higher energy by at least 4000 cm^{-1}.

However, although this CT state experiences the largest ESAF, it is not the state which mixes the most with the GS as the corresponding transfer elements are smaller than those of the out-of-plane oxo $p_x \rightarrow$ Fe xz CT transitions which make a larger contribution to the GS coupling; these are located in the region from 26 000–28 400 cm^{-1}. The 'inverted' assignment of the lowest-energy CT transition being an in-plane and not an out-of-plane transition accounts for the observation that although the intensity of the 20 500 cm^{-1} band is a factor of two lower than those of the higher-energy CT bands, it shows the highest Raman enhancement: a transition from the more bonding orbital, the in-plane pπ, should result in a larger distortion in the excited state and thus lead to a greater resonance enhancement than a transition from a less bonding, out-of-plane pπ-orbital. There are also interference effects between excited states. Finally, the observed ferromagnetism in the $^4A_1$ excited state also can be understood based on the dominance of the π/σ pathways. These are the only antiferomagnetic pathways whose contribution to exchange is expected to decrease in the excited state and thus promote ferromagnetism. The mixed π/σ interactions only become important upon bending the Fe–O–Fe unit from 180° and explain the limited angular dependence of J in the Fe–O–Fe dimer systems.

8. VBCI parameters of homovalent systems applied to the corresponding one-electron reduced binuclear complexes: relevance to electron transfer [16]

The VBCI parameters determined in the analysis of a homovalent transition-metal dimer can be used to determine the electronic coupling matrix element in the corresponding one-electron reduced, mixed-valent (MV) species. This is important for correlating exchange coupling to superexchange pathways for electron transfer (ET). It can be shown that knowledge of the ground-state $-2J$ value for the homodimer is sufficient.

To this end, it is useful to express the metal–ligand transfer matrix elements h_{dL} in terms of a metal–metal transfer matrix element H_{AaBb}:

$$H_{A_aB_b} = 2h_{dL}^2/\Delta \tag{13}$$

Note that that a and b correspond to orthogonalized orbitals localized on A and B which contain contributions of the ligands including the bridging one. Strictly, transformation Eq. (13) corresponds to a symmetric pathway a(A)–(h_{aL})–L–(h_{bL})–b(B) where only one CT energy Δ is involved. In the following discussion, it is therefore assumed that a = b. Thus,

$$H_{A_aB_b} \equiv H_{AB} \tag{14}$$

In terms of H_{AB}, the ground-state coupling constant $-2J$ for, e.g. a Cu(II)–Cu(II) system is found to be (cf. Eq. (8)) [35]

$$-2J = (H_{AB})^2/U \tag{15}$$

The GS-MMCT mixing coefficient is given by

$$c_{AB} = 2h_{dL}^2/(\Delta \cdot U) = H_{AB}/U \tag{16}$$

Now, instead of the four-electron system used in Section 4, a five-electron system is considered where the additional electron is located in a metal orbital; i.e. one metal site is singly, the other one doubly occupied, and the ligand orbital is doubly occupied as well. If the electron is more or less localized at one site, a GS-MMCT mixing (or valence delocalization) coefficient can be formulated as

$$c_{AB}^{MV} = (h'_{dL})^2/(\Delta \cdot U') \equiv H_{AB}^{MV}/U' \tag{17}$$

where h'_{dL} corresponds to the transfer matrix element in the mixed-valent (MV) dimer and U' is now the energy of the MMCT state *in the localized limit*, i.e. the energy of the intervalence CT band. Note that this IVCT energy U' can be much smaller than the Mott–Hubbard U of the corresponding homovalent system (e.g. Cu(I)–Cu(II) vs. Cu(II)–Cu(II)). By comparison of Eqs. (16) and (17)

$$H_{AB}^{MV} = \frac{1}{2}\frac{(h'_{dL})^2}{h_{dL}^2}H_{AB} \cong \frac{1}{2}H_{AB} \tag{18}$$

where the factor of (1/2) in H_{AB}^{MV} relative to H_{AB} is due to the loss of the twofold symmetry of the homovalent dimer. In the MV system the matrix element H_{AB}^{MV} gives rise to an energetic stabilization of the minimum of the local potential in the order of

$$h_{dL}^4/(\Delta^2 \cdot U') = (H_{AB}^{MV})^2/U' \tag{19}$$

whereas at the intersection point of the two local potentials, an energetic splitting between the upper and the lower potential surfaces of

$$E_{upper} - E_{lower} = 2H_{AB}^{MV} \tag{20}$$

results (Fig. 22). This allows an estimate of how the classical activation barrier for ET is lowered. Brunold et al. have applied this method to the π/σ pathway in the

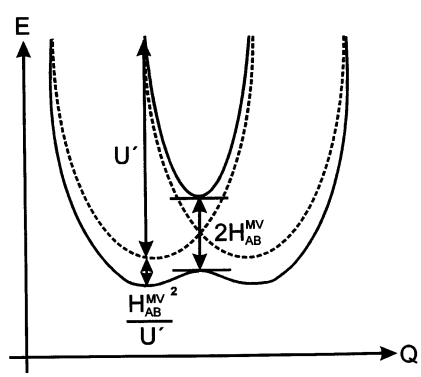

Fig. 22. Potential energy surface of a symmetric mixed-valent dimer indicating the splitting of the two hypersurfaces at the crossing point of the two parabolas and the lowering of the local minima and the classical activation barrier, respectively, due to the electronic coupling matrix element H_{AB}^{MV}.

Fe–O–Fe dimer (cf. Section 7) and estimated that H_{AB} ca. 312 000 cm^{-1} and therefore H_{AB}^{MV} ca. 46000 cm^{-1}. Therefore ET in oxy-Hr must proceed adiabatically [16]. Thus, the H_{AB}^{MV} estimated by Eq. (18) from the measured ground-state J value and U of the homodimer (Eq. (15)) can be used in the non-adiabatic limit in Marcus theory to estimate k_{ET}.

9. Summary and conclusions

The present overview summarizes a series of papers which have contributed to our present understanding of excited-state interactions in transition-metal dimers. Of course, this compilation reflects the perspective of the authors. The common theme is an investigation of superexchange both in the ground state and excited states of binuclear complexes with the goal of physically understanding the origin of these interactions, the correlation between excited and ground-state coupling and the relation of superexchange pathways for exchange to electron transfer.

On a phenomenological basis, exchange effects are taken into account by a coupling constant J in the electronic ground state or an excited state which has the same configuration as the ground state. If these J values are not very small (i.e. in the order of several cm^{-1}), orbital overlap via bridging ligands is necessarily involved. In a more general picture which includes interconfigurational transitions, a phenomenological description of excited-state interactions is obtained in terms of a set of four integrals of exciton theory, K, J, I and L. Again, these integrals describe interactions between single-site orbitals n_A and m_B, delocalized more or less towards each other (n_A and m_B are d-orbitals on center A and B, respectively). Note that for more than one unpaired electron per site, the (Heisenberg) ground-state J can be composed of several $J(n_A,m_B)$ interactions. The same holds for (spin-flip) excited-state Js in terms of the Tanabe model. We have referred to this description as 'weak' coupling as it remains within the manifold of metal-centered d-orbitals, in the spirit of LF theory.

The *physical origin* of a specific orbital coupling constant $J(n_A,m_B)$ is found by considering the states deriving from transfer of an electron to n_A or m_B from the ligand orbital(s) bridging n_A and m_B, i.e. the *charge-transfer states* being involved in transfer of the electron from n_A to m_B. Evaluation of the energy shifts and splittings present in these states provides a *microscopic view* on the corresponding $n_A \leftrightarrow m_B$ superexchange interaction. This is the domain of the VBCI model ('strong coupling'). In this model the magnetic (e.g. singlet/triplet) and dimer (g/u) splittings of excited states derive from configuration interaction with LMCT and MMCT states. This way, *covalency* is explicitly taken into account. Again, a particular $J(n_A,m_B)$ constant may be composed of several terms corresponding to ferro- and AF contributions. Thus the VBCI treatment determines the individual superexchange pathways contributing to a particular $J(n_A, m_B)$ and thus provides the highest possible information regarding a specific orbital interaction in the dimer. This applies both to the ground state or a LF excited state. Note that due to orbital occupancy a $J(n_A, m_B)$ interaction may give an AF contribution in the ground and

a ferromagnetic contribution in the excited state or vice versa. Finally, the determination of a transfer matrix element involved in superexchange can directly be associated with the corresponding electron pathway in the one-electron reduced intermediate and thus provides the electronic coupling matrix element H_{AB} for ET in Marcus theory. Clearly, more applications of this method are expected.

Acknowledgements

This research was supported by the NIH DK31450 and NSF MCB-9816051 (to E.I.S.).

References

[1] R.D. Willett, D. Gatteschi, O. Kahn (Eds.), Magneto-Structural Correlations in Exchange Coupled Systems, Reidel, Dordrecht, 1985.
[2] A.B.P. Lever, Inorganic Electronic Spectroscopy, Elsevier, New York, 1984.
[3] A.E. Hansen, C.J. Ballhausen, Trans. Faraday Soc. 61 (1965) 631.
[4] L. Dubicki, Aust. J. Chem. 25 (1972) 1141.
[5] S.R. Desjardins, D.E. Wilcox, R.L. Musselman, E.I. Solomon, Inorg. Chem. 26 (1987) 288.
[6] (a) H.J. Schugar, G.R. Rossman, C.G. Barraclough, H.B. Gray, J. Am. Chem. Soc. 94 (1972) 2683; (b) H.J. Schugar, G.R. Rossman, J. Thibeault, H.B. Gray, Chem. Phys. Lett. 6 (1970) 26.
[7] C.A. Brown, G.J. Remar, R.L. Musselman, E.I. Solomon, Inorg. Chem. 34 (1995) 688.
[8] (a) D.S. McClure, J. Chem. Phys. 39 (1963) 2850;
(b) L.L. Lohr, D.S. McClure, J. Chem. Phys. 49 (1968) 3516;
(c) J. Ferguson, H.J. Guggenheim, Y. Tanabe, J. Phys. Soc. Jpn. 21 (1966) 692;
(d) R.S. Meltzer, M. Lowe, D.S. McClure, Phys. Rev. 180 (1969) 561.
[9] R. Schenker, H. Weihe, H.U. Güdel, Inorg. Chem. 38 (1999) 5593 (and references therein).
[10] P.K. Ross, M.D. Allendorf, E.I. Solomon, J. Am. Chem. Soc. 111 (1989) 4009.
[11] E.I. Solomon, M.J. Baldwin, M.D. Lowery, Chem. Rev. 92 (1992) 521.
[12] E.I. Solomon, F. Tuczek, D.E. Root, C.A. Brown, Chem. Rev. 94 (1994) 827.
[13] E.I. Solomon, U.M. Sundaram, T.E. Machonkin, Chem. Rev. 96 (1996) 2563.
[14] J.E. Pate, P.K. Ross, T.J. Thamann, C.A. Reed, K.D. Karlin, T.N. Sorrell, E.I. Solomon, J. Am. Chem. Soc. 111 (1989) 5198.
[15] F. Tuczek, E.I. Solomon, Inorg. Chem. 32 (1993) 2850.
[16] T.C. Brunold, D.R. Gamelin, E.I. Solomon, J. Am. Chem. Soc. 122 (2000) 8511.
[17] H.J. Schugar, E.I. Solomon, W.L. Cleveland, L. Goodman, J. Am. Chem. Soc. 97 (1975) 6442.
[18] B. Bleaney, K.D. Bowers, Proc. R. Soc. London Ser. A 214 (1952) 451.
[19] A.E. Hansen, C.J. Ballhausen, Trans. Faraday Soc. 61 (1965) 631.
[20] (a) O. Kahn, B. Briat, J. Chem. Soc. Faraday Trans. 2 72 (1976) 268;
(b) O. Kahn, B. Briat, J. Chem. Soc. Faraday Trans. 2 72 (1976) 1441.
[21] D.P. Craig, S.H. Walmsley, Excitons in Molecular Crystals, Benjamin, New York, 1968.
[22] Y. Tanabe, K. Aoyagi, in: E.I. Rashba, M.D. Sturge (Eds.), Excitons, North-Holland, Amsterdam, 1982, pp. 603–663.
[23] F. Tuczek, E.I. Solomon, J. Am. Chem. Soc. 116 (1994) 6916.
[24] E. Pidcock, V. Obias, M. Abe, H.-C. Liang, K.D. Karlin, E.I. Solomon, J. Am. Chem. Soc. 121 (1999) 1299.
[25] (a) K.D. Karlin, R.W. Cruse, Y. Gultneh, A. Farooq, J.C. Hayes, J. Zubieta, J. Am. Chem. Soc. 109 (1987) 2668;
(b) J.E. Pate, R.W. Cruse, K.D. Karlin, E.I. Solomon, J. Am. Chem. Soc. 109 (1987) 2624.

[26] K.A. Magnus, H. Ton That, J.E. Carpenter, Chem. Rev. 94 (1994) 727.
[27] N. Kitajima, K. Fujisawa, Y. Moro-oka, K. Toriumi, J. Am. Chem. Soc. 111 (1989) 8975.
[28] N. Kitajima, K. Fujisawa, C. Fujimoto, Y. Moro-oka, S. Hashimoto, T. Kitagawa, K. Toriumi, K. Tatsumi, A. Nakamura, J. Am. Chem. Soc. 114 (1992) 1277.
[29] A.G. Blackman, W.B. Tolman, Struct. Bonding (Berlin) 97 (2000) 179.
[30] F. Tuczek, Spectroscopic Methods in Bioinorganic Chemistry, ACS Books, American Chemical Society, Washington, DC, 1998.
[31] S.V. Didziulis, S.L. Cohen, A.A. Gewirth, E.I. Solomon, J. Am. Chem. Soc. 110 (1988) 250.
[32] P.K. Ross, E.I. Solomon, J. Am. Chem. Soc. 113 (1991) 3246.
[33] I. von Seggern, F. Tuczek, W. Bensch, Inorg. Chem. 34 (1995) 5530.
[34] D.R. Gamelin, E.L. Bominaar, C. Mathonière, M.L. Kirk, J.-J. Girerd, K. Wieghardt, E.I. Solomon, J. Am. Chem. Soc. 118 (1996) 8085.
[35] Note that $H_{A_aB_b}$ corresponds to $2h_{ab}$ in: P.J. Hay, J.C. Thibeault, R. Hoffman, J. Am. Chem. Soc. 97 (1975) 4884.